Effect of topological length on bound state signatures in a topological nanowire

Dibyajyoti Sahu,* Vipin Khade, and Suhas Gangadharaiah†
Department of Physics, Indian Institute of Science Education and Research, Bhopal, India

(Received 28 November 2022; revised 2 November 2023; accepted 6 November 2023; published 27 November 2023)

Majorana bound states (MBSs) at the end of nanowires have been proposed as one of the most important candidates for topological qubits. However, similar tunneling conductance features for both the MBSs and Andreev bound states have turned out to be a major obstacle in the verification of the presence of MBSs in semiconductor-superconductor heterostructures. In this article, we use a protocol to probe properties specific to the MBSs and use it to distinguish the topological zero-bias peak (ZBP) from a trivial one. For a scenario involving a quantized ZBP in the nanowire, we propose a scheme wherein the length of the topological region in the wire is altered. The tunneling conductance signatures can then be utilized to gauge the impact on the energy of the low-energy states. We show that the topological and trivial ZBPs behave differently under our protocol; in particular, the topological ZBP remains robust at zero bias throughout the protocol, while the trivial ZBP splits into two peaks at finite bias. This protocol probes the protection of near-zero-energy states due to their separable nature, allowing us to distinguish between topological and trivial ZBP.

DOI: 10.1103/PhysRevB.108.205426

I. INTRODUCTION

The Kitaev one-dimensional (1D) topological superconducting model [1] predicts Majorana modes at the ends of the 1D chain. These well-separated states form robust nonlocal fermionic states and in addition under braiding the Majorana states obey non-Abelian statistics, thus potentially providing an ideal base for fault-tolerant topological quantum computation [2–4]. Since then a number of theoretical proposals have been made for potentially realizing systems that could host the Majorana modes. Some of the earliest proposals include fractional quantum Hall states at filling $\nu = 5/2$ [5], and spinless topological $p_x + ip_y$ superconductors with the cores hosting Majorana modes [6]. Others include the cores of superconducting vortices present on the surface of a three-dimensional (3D) topological insulator proximitized to an s-wave superconductor [7], a semiconductor film with spin-orbit interaction and proximity coupled to an s-wave superconductor and magnetic field [8], and a quantum wire with strong spin-orbit interaction proximity coupled to a superconductor in the presence of magnetic field [9,10] which drives the system from a trivial phase with a finite gap to a topological phase containing a zero-energy Majorana bound state (MBS) in the gap. Intensive experimental efforts have been made in realizing the above setups; in particular, the last setup involving InAs, InSb, and other quantum wires has been quite promising [11–14].

Of all the signatures of MBSs, the overwhelming emphasis has been on experimentally detecting the zero-bias tunneling conductance and its corresponding interpretation [15–45]. From the theoretical perspective, tunneling at the edge of the topological superconductor (where the MBSs are localized) results in a resonant effect; consequently the zero-bias peak (ZBP) conductance is expected to acquire the quantized value of $2e^2/h$ [15]. Previous studies have shown that the ZBP can also appear due to the Andreev bound states (ABSs), with the peak height close to the quantization values [18,25,26]. The origin of ABSs is often due to inhomogeneous profiles and quantum dots at the wire's end and many times they mimic MBS tunneling signatures. The typical ABS consists of overlapping Majorana components, making them very sensitive to parameter changes. Therefore, the ZBP due to the ABS can generally be attributed to the fine tuning of the parameters and hence is not robust [46]. Recent theoretical works have shown that the trivial in-gap states can actually be pinned close to zero energy for an extended range of parameter space for certain inhomogeneous profiles, making the ZBP robust. These ABSs have their Majorana components partially separated (termed as the ps-ABS) from each other [47]. On the other hand, for magnetic field strengths greater than the critical value, the wire will be in the topological regime wherein the Majorana components are completely separated and localized at the two ends of the wire. It turns out that the ps-ABS appear just before the critical Zeeman term [48]; thus it is challenging to unambiguously pin the origin of the ZBP as arising from either the topological or the trivial states.

To distinguish them, use of two leads each placed at the opposite ends of the wire have been proposed as they can measure the correlations between the conductance from the two local leads. In addition, this setup can be used to probe nonlocal conductances which arise due to the bulk states and can produce the band gap closing signature at the topological phase transition point beyond which the MBS appears [46,49]. However, as discussed in Ref. [50], the presence of inhomogeneities like quantum dots at both ends can yield correlated trivial ZBPs in both the local conductances. It turns out that

*dibyajyoti20@iiserb.ac.in
†suhasg@iiserb.ac.in

the nonlocal conductance signatures in the case of the heterostructures are not strong enough to unambiguously depict the band gap closing. Besides the above, dephasing, leakage dynamics of Majorana modes [51], recent studies focused on the robustness of quantization of ZBPs with respect to tunneling barrier height and temperature [52], and phase-biased Josephson currents [53–55] have been suggested as potential schemes to distinguish the topological Majorana modes from the Andreev states.

As mentioned in the preceding paragraph the presence of quantized ZBPs is insufficient to conclude the existence of MBSs because trivial ABSs can also produce quantized ZBPs. To distinguish topological states from normal zero modes, one needs to go beyond the presence of quantized ZBPs and probe properties specific to MBSs only. Consider that the ends of the wire are moved into a trivial parameter space which effectively changes the topological length (i.e., the length of region whose parameters are in the topological regime); in such a case, one produces a trivial-topological-trivial structure with the MBS still present at the edge of the topological region. This property specific to the MBS has been proposed before for Majorana braiding protocols [4,56–58] and probing [54]. Motivated by this, we define the “moving protocol” to systematically decrease the topological length by fixing the wire’s ends in a parameter regime below the topological range by either reducing the Zeeman term or the external potential. We employ the “Zeeman moving protocol” (ZMP) by applying a Zeeman term profile and the “potential moving protocol” (PMP) with external potential in our numerical simulation. Since local conductance measures the local property of the wire close to the lead, the effect of change in the topological region should be apparent in the local conductance. We apply both protocols to diverse scenarios and investigate their impact on the trivial and the topological ZBPs. We show that the topological ZBP from MBSs remains robust under the moving protocol. At the same time, the trivial ZBP from the ps-ABS has entirely different behavior, splitting into two separate peaks at finite bias. This difference in behavior arises due to the fundamental difference between the MBS and ps-ABS in the overlap of their Majorana components. Our “moving protocol” indirectly probes this separable nature of the Majorana components. We also show that the PMP is more effective compared to the ZMP as far as distinguishing trivial and topological ZBPs is concerned.

The organization of the paper is as follows. In Sec. II, we describe the model and profile of the semiconductor-superconductor nanowire used to produce the different heterostructures. In this section, we also define our moving protocols, under which we will study tunneling conductance signatures. In Sec. III, we present our results. First, we look into a homogeneous nanowire and its tunneling conductance signatures. We also look at the inhomogeneous system, which can have both trivial and topological ZBPs. We show the effect of the ZMP on the trivial and topological ZBPs to demonstrate the different ways they behave. In Sec. III C, we present the behavior of topological and trivial ZBPs under the PMP. In Sec. III D, we consider another system, S′SS′ (where S′ and S are superconducting regions of the wire with different chemical potential), to showcase the shortcomings of the ZMP and how we go around it by using the PMP to distinguish topological ZBPs from trivial ZBPs. Finally, we present our conclusions in Sec. IV.

II. MODEL

We study a 1D semiconductor nanowire with spin-orbit coupling having a superconducting gap induced via the proximity effect. In addition, we take into consideration a magnetic field applied perpendicular to the wire and parallel to the superconductor. The corresponding Hamiltonian which incorporates all of the above terms is given by

$$H = -\sum_{n}\left\{\left[\sum_{\sigma,\sigma'} c^{\dagger}_{n+1,\sigma}\left(t_n\delta_{\sigma,\sigma'} - i\alpha_n\sigma^{z}_{\sigma,\sigma'}\right)c_{n,\sigma'} + c^{\dagger}_{n,\sigma}\frac{\left(-\mu_n\delta_{\sigma,\sigma'} + \Gamma\sigma^{y}_{\sigma,\sigma'}\right)}{2}c_{n,\sigma'}\right] + \Delta_n c^{\dagger}_{n,\uparrow}c^{\dagger}_{n,\downarrow} + \text{H.c.}\right\}, \tag{1}$$

where $c^{\dagger}_{n,\sigma}$ $(c_{n,\sigma})$ represents the creation (annihilation) operator of fermions with spin σ at site n. The parameters t_n, α_n, μ_n, Γ, and Δ represent the tunneling, spin-orbit coupling, chemical potential, Zeeman energy, and the superconducting terms, respectively, at the site n. δ denotes Kronecker delta. This will be our base model on top of which different profiles of μ_n and Δ_n are added to create different heterostructures. We will focus our attention on the following two scenarios. The first one is the homogeneous case in which all the parameters in the Hamiltonian are taken to be position independent. We reproduce the result of this well-studied parameter regime to validate our numerical scheme and to interpret the effect of our protocol on this system. In the second scenario we will consider the presence of smooth variation in the Δ_n and μ_n profiles. The latter differentiates the different chemical potential in the normal (N) regions and the superconductor (S) regions, while the former creates regions of N and S resulting in NS- and NSN-type heterostructures. For certain parameter regimes these heterostructures can host ABSs or quasi-MBSs, which can stay close to zero energy over a large range of magnetic fields. The smooth variation of the spatial profile is modeled by the function [46,49,50]

$$\Omega_{n_0,s}(n) = \frac{1}{2}\left[1 + \tanh\left(\frac{n-n_0}{s}\right)\right] \tag{2}$$

where n_0 represents the point around which the profile changes, while s is a measure of smoothness in the variation (which has been fixed to $s = 20$ for all profiles).

For example, an NS profile with smoothly varying chemical potential can be represented via the following set of parameters:

$$\Delta_n = \Delta_0\Omega_{N_1,s}(n),$$
$$\mu_n = \mu_N + (\mu_S - \mu_N)\Omega_{N_1,s}(n), \tag{3}$$

where N_1 is the length of the normal region in the heterostructure; μ_S and μ_N are the chemical potential for the S and N regions, respectively; and Δ_0 is the effective superconducting coupling strength in the S region. The NSN heterostructure can be modeled by the following set of parameters with the

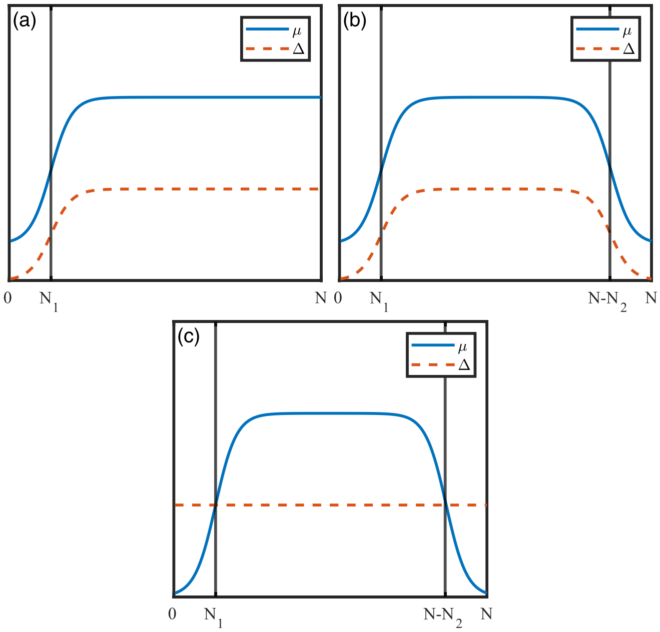

FIG. 1. Plots of the inhomogeneous profile for (a) NS, (b) NSN, and (c) S′SS′ systems.

profile given by

$$\begin{aligned}\Delta_n &= \Delta_0[\Omega_{N_1,s}(n) - \Omega_{N_1+N_S+1,s}(n)],\\ \mu_n &= \mu_{N_1} + (\mu_S - \mu_{N_1})\Omega_{N_1,s}(n)\\ &\quad + (\mu_{N_2} - \mu_S)\Omega_{N_1+N_S+1,s}(n),\end{aligned} \tag{4}$$

where μ_{N_1} and μ_{N_2} are the chemical potentials for the normal regions. We note that N_1, N_2, and N_S, denote the length of left and right normal regions and the superconducting region, respectively. Together with these systems we also consider S′SS′ which has a homogeneous Δ but inhomogeneity in μ, which distinguishes the two superconducting regions S′ and S:

$$\begin{aligned}\Delta_n &= \Delta_0,\\ \mu_n &= \mu_S[\Omega_{N_1,s}(n) - \Omega_{N_1+N_S+1,s}(n)].\end{aligned} \tag{5}$$

Plots of the NS, NSN, and S′SS′ systems μ and Δ profile are shown in Fig. 1.

As a simple diagnostic tool to distinguish the presence of MBSs from the ABSs in the various parameter regimes we calculate the boundary topological invariant (TI) using the scattering matrix S. The scattering matrix relates the incoming and outgoing wave amplitudes:

$$S = \begin{pmatrix} R & T' \\ T & R' \end{pmatrix}. \tag{6}$$

Note that the reflection subblocks R, R' and the transmission subblocks T, T' connect the two ends of the chains and are obtained in terms of the Fermi level wave amplitudes. $\mathrm{TI} = \mathrm{sgn}\,\mathrm{Det}(R) = \mathrm{sgn}\,\mathrm{Det}(R')$ obtains a value of $+1$ when the wire is in the trivial phase and -1 for the topological phase [59] (further details are provided in Appendix A). Along with the topological invariant we also plot the wave function of the Majorana components to characterize the topological nature of the bound states. The Hamiltonian has particle-hole symmetry, giving rise to a symmetric spectrum with two fermionic wave functions $\Psi_\epsilon(x)$ and $\Psi_{-\epsilon}(x)$ for every eigenvalue ϵ. Thus one constructs the following symmetric and antisymmetric wave functions from the low-energy eigenstates [60]:

$$\begin{aligned}\gamma_1(x) &= \frac{1}{\sqrt{2}}[\Psi_\epsilon(x) + \Psi_{-\epsilon}(x)],\\ \gamma_2(x) &= \frac{i}{\sqrt{2}}[\Psi_\epsilon(x) - \Psi_{-\epsilon}(x)].\end{aligned} \tag{7}$$

The wire can thus be characterized as topological (with MBS) if $\gamma_1(x)$ and $\gamma_2(x)$ are spatially separated, while the overlapping and partially overlapping states characterize ABS and ps-ABS, respectively [46,52].

We perform tunneling conductance calculations for a setup involving two normal leads attached to either side of the wire to create a three-terminal device (see Fig. 2) [49]. The conductance matrix has the following form:

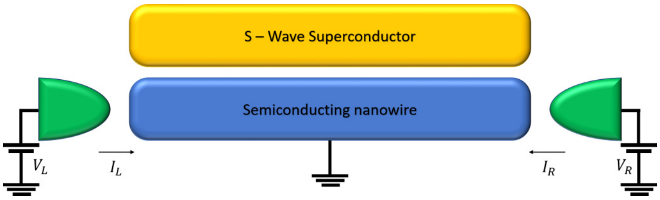

FIG. 2. Tunneling conductance setup with two leads.

$$G = \begin{pmatrix} G_{\mathrm{LL}} & G_{\mathrm{LR}} \\ G_{\mathrm{RL}} & G_{\mathrm{RR}} \end{pmatrix}, \tag{8}$$

where the elements of the matrix are given by

$$G_{ij} = \left.\frac{dI_i}{dV_j}\right|_{V_i=0}. \tag{9}$$

The local and the nonlocal conductances are calculated using the Green's function method. Details related to the calculations are provided in Appendix B. We focus our attention on the effect the topological length of the wire has on the tunneling conductance signatures. In our setup, by appropriately choosing site-dependent Zeeman or chemical potential terms, different regions of the 1D wire can be tuned to be in the topological or the trivial phase [4,56]. Consider the following spatially dependent Zeeman strength,

$$\Gamma_n = \Gamma_0 \mathrm{F}(n, n_0, N, s'),$$

where

$$\mathrm{F}(n, n_0, N, s') = n_F\left[2\left(\frac{n_0 - n}{s'}\right)\right] n_F\left[2\left(\frac{n - N + n_0}{s'}\right)\right],$$

and $n_F(x) = 1/(1 + e^x)$, where N represents the total number of sites of the nanowire and s' is smoothness parameter (fixed to $s' = 10$). A sample plot of the profile is shown in Fig. 3(a) for $n_0 = 50$. For the protocol that we consider, Γ_0 is kept unchanged while n_0 is increased from negative to positive values. If Γ_0 is above the critical field, the wire will be topological for approximately $n_0 < n < N - n_0$ regions. Thus, increasing n_0 decreases the length of the topological region due to the

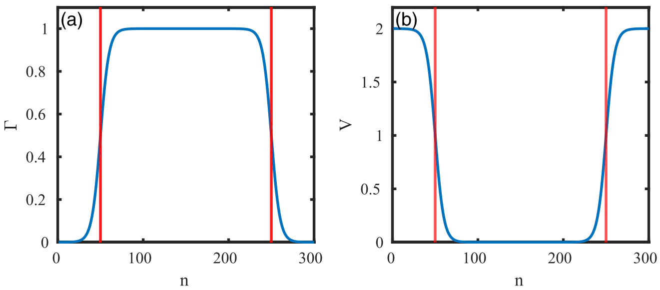

FIG. 3. Moving protocol profile for $N = 300$ and $n_0 = 50$ (a) with Zeeman profile (ZMP) for $\Gamma_0 = 1$ and (b) with external potential (PMP) profile for $V_0 = 2$.

Zeeman strength being below the critical values in those regions. For $\Gamma_0 > \Gamma_c$ this profile creates a domain-wall structure of trivial-topological-trivial superconductor; changing n_0 thus results in the change of the topological length. We denote this protocol of changing the topological length as the Zeeman moving protocol and we will be exploring the effect it has on the ZBP due to the presence of either the ps-ABS or the MBS. In addition to the Zeeman term, one could also use tunable local gates to add an external potential which increases the effective chemical potential in the ends of the wire to put them in a trivial state, thus decreasing the topological length. To consider this we will add external potential of the form of Eq. (10) to our chemical potential, the plot of which is shown in Fig. 3(b):

$$V_n = V_0(1 - F(n, n_0, N, s')). \tag{10}$$

We denote this protocol of changing the topological length as the potential moving protocol.

III. RESULTS

In this section, we will be considering the effects of the moving protocol on the ZBP for the homogeneous and inhomogeneous systems. For either of them, we begin by exploring the phase diagram by calculating the topological boundary invariant. Furthermore, we calculate the Majorana components to classify the in-gap states. We reproduce some of the earlier results on the ZBP by calculating the tunneling conductance. The main thrust of our work is to distinguish the ZBP arising due to the presence of topological and trivial bound states via the moving protocol.

A. Homogeneous system

We choose the parameter space of InSb-Al nanowire, which is often used in theoretical and experimental studies [46,49]. The effective mass considered is $m^* = 0.015m_e$ with lattice constant $a = 10$ nm and Rashba spin-orbit coupling $\alpha_R = 0.4$ eVÅ, which yields $t = \hbar^2/2m^*a^2 = 25.4$ meV and $\alpha = \alpha_R/2a = 2$ meV. The effective superconducting coupling term considered is $\Delta = 0.5$ meV [49,52]. The ideal system enters the topological nontrivial region when the Zeeman strength is greater than the critical value given by $\Gamma_c \approx \sqrt{\mu^2 + \Delta^2}$. Using the scattering matrix approach, we have calculated the TI for a range of μ and Γ, and as shown

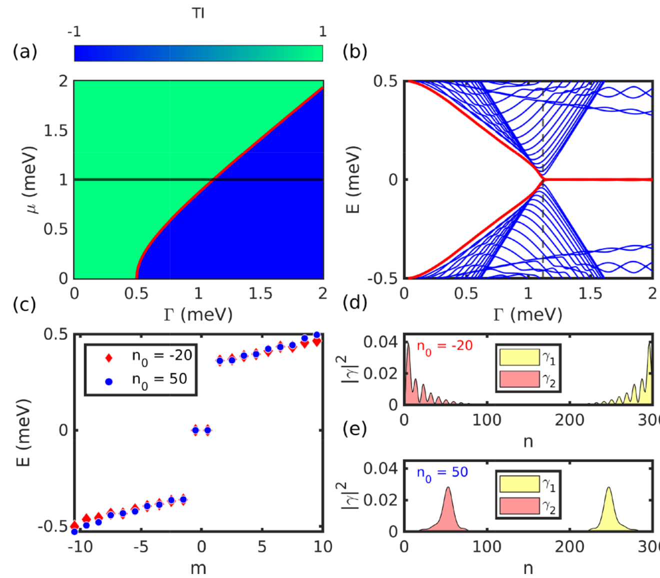

FIG. 4. Homogeneous system with parameters $t = 25.4$ meV, $\alpha = 2$ meV, and $\Delta = 0.5$ meV. (a) Phase portrait with boundary topological invariant for range of μ and Γ values; the red line denotes the critical Zeeman term for each μ value separating topological (TI $= -1$) and trivial (TI $= 1$) phases. (b) Energy spectrum for $\mu = 1$ meV showing MBS after Γ_c (vertical grey dash line). (c) Energy eigenvalues (index m) with moving profile for different n_0 values. (d) Majorana components of low-energy states at $\Gamma_0 = 1.5$ meV for different instances of moving protocol. It shows MBSs moving away from the ends.

in Fig. 4(a) the numerically obtained boundary between the topological and the nontopological region coincides with the theoretical prediction of the critical field shown by the red curve. For concreteness, we consider $\mu = 1$ meV as the on-site potential; the corresponding critical Zeeman strength for which the band closing takes place is $\Gamma_c \approx 1.12$ meV. From the plot of energy spectrum vs Γ shown in Fig. 4(b), we observe the expected appearance of zero-energy modes after the band closing which takes place at the critical Zeeman field.

The numerically calculated tunneling conductance for a range of Γ is plotted in Fig. 5. It is clear from the figure that a ZBP in the local conductance appears after Γ_c. The ZBP is quantized at $2e^2/h$ which is also the predicted conductance for the MBS. The left (G_{LL}) and right (G_{RR}) local conductances exhibit coherence, denoting the presence of MBSs on either ends of the nanowire and at the same time the nonlocal conductances G_{LR} and G_{RL} exhibit the signature of band-gap closing. These tunneling conductance signatures arising from an ideal nanowire with MBSs at the edges of the pristine nanowire have been well studied in the past literature [49,52].

Before we discuss the effect of the ZMP on the ZBP, we will first explore its effect on the system's energy levels. The results of the spectrum under the ZMP for two different values of n_0 are shown in Fig. 4(c). From the plot of the energy spectrum it is clear that the MBSs remain fixed at zero energy since the protocol only changes the length of the topological region by putting some part of the wire in a Zeeman term below the critical term (Γ_c). As long as the length of the topological region remains much larger than the Majorana localization

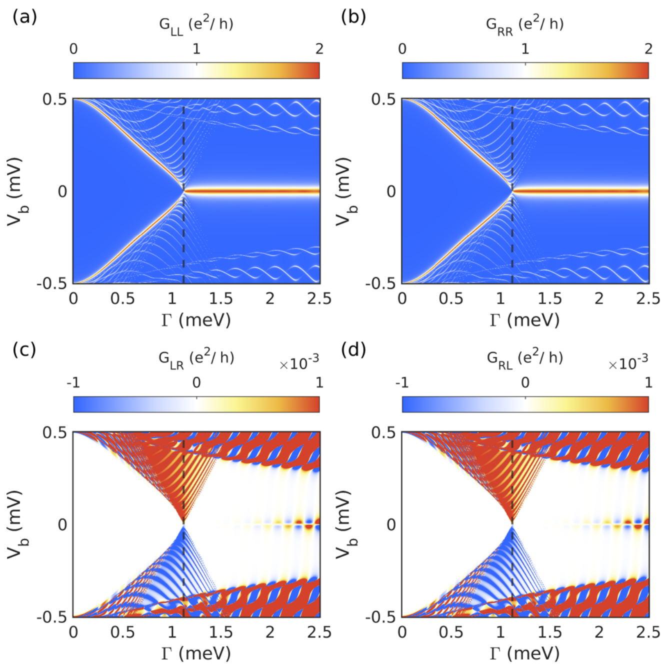

FIG. 5. [(a), (b)] Local and [(c), (d)] nonlocal tunneling conductance for the homogeneous system; the grey dashed line denotes the critical Zeeman term. Local conductance shows the presence of ZBPs and the nonlocal conductance captures the band closing signature.

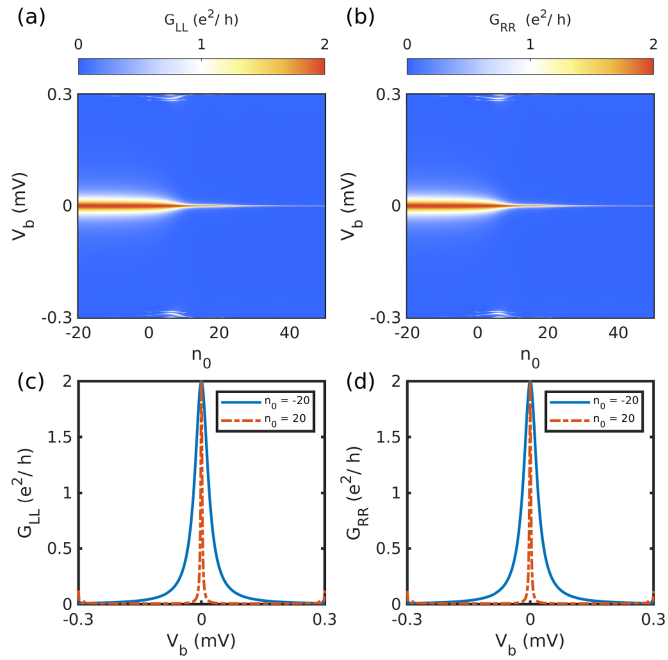

FIG. 6. Tunneling conductance signature on the application of the ZMP with $\Gamma_0 = 1.5$ meV. [(a), (b)] Local tunneling conductance for a range of n_0 values and [(c), (d)] vertical line cut of conductance for specific n_0. Both local conductance values show robustness of the topological ZBP under ZMP.

length, the energies of the MBSs will be fixed at zero energy due to the topological protection. Further insight into the effect of the protocol on the state is obtained by plotting the Majorana components of the low-energy states. For a uniform Zeeman term (which is the case for $n_0 = -20$) the MBSs are localized at the edges of the nanowire with the two Majorana components spatially separated [see Fig. 4(d)]. However, as the Zeeman term profile is moved so that $n_0 = 50$, the length of the topological region as well as the bound state position change but at the same time they remain localized at the edges of the topological region as shown in Fig. 4(e). The Majorana components are still separated so they stay at zero energy.

We next focus the effect of the ZMP on the ZBP. For the ZMP, the calculated local conductance for a range of n_0 can be seen in Figs. 6(a) and 6(b). As n_0 is increased (i.e., the topological region is reduced while the position of the lead remains unchanged), a subsequent decrease in the width of the ZBP becomes apparent, while at the same time the height of the peak remains quantized to the value $2e^2/\hbar$. We also plot the value of the conductance for two values of n_0 in Figs. 6(c) and 6(d), where the quantization of the peak is clearly observed. This feature has a simple explanation due to the property of the MBS. Application of the moving protocol changes the topological length of the wire and therefore the MBS moves farther away from the lead while always staying at the edge of the topological region. Since the edge states move farther away from the lead the coupling between the lead and the MBS decreases, resulting in the reduced width of the ZBP. For sufficiently large separation between the lead and the edge mode, the ZBP disappears altogether. Throughout this protocol the Majorana components remain spatially separated; as a result the MBS remains at zero energy, causing the peak to be at zero bias through out this protocol.

B. Inhomogeneous wire

In quantum wires it is difficult to achieve a scenario wherein the parameters are homogeneous throughout the length of the wire. Instead, the inhomogeneous profile in the heterostructure better captures the realistic scenario. Specifically, the presence of quantum dots creates a situation where the chemical potential at the edges is lower compared to the interior of the wire [46,49,50]. To account for this, we consider an inhomogeneous NS heterostructure in our analysis. The chemical potential and the superconducting profile that model this heterostructure are represented by Eq. (3) and illustrated in Fig. 1(a), respectively.

The numerically calculated topological boundary invariance is shown in Fig. 7(a), which shows the presence of the topological phase for Zeeman terms greater than Γ_c for a given value of the chemical potential (in the S region). This figure is similar to the corresponding Fig. 4(a) for the homogeneous case. However, the difference between the two scenarios can be seen from the presence of low-lying energy states close to zero energy even in the nontopological regime [see Fig. 7(b)]. It turns out that the zero-energy modes in the trivial region persist for large ranges of Zeeman coupling and chemical potential. The energy spectrum for the system for $\mu = 1$ meV is shown in Fig. 7(c), which shows the appearance of the ABS before the topological phase transition at $\Gamma_c \approx 1.12$ meV. For $\Gamma > \Gamma_c$ the Majorana components obtained from the low-lying states are completely separated and localized at the edges and represent the MBSs [see Fig. 7(e)],

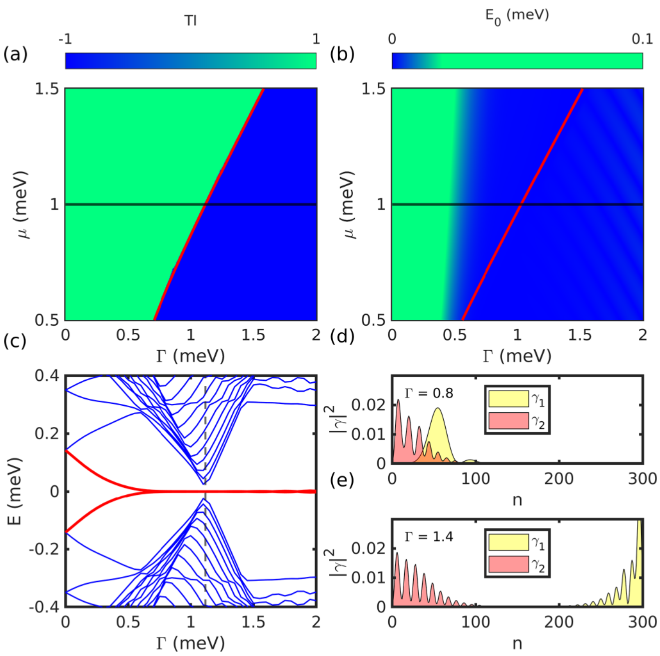

FIG. 7. NS system with parameters $t = 25.4$ meV, $\alpha = 2$ meV, $\Delta_0 = 0.5$ meV, $N_1 = 40$, $\mu_N = 0.2$ meV, and $N = 300$. Phase portrait for a range of chemical potentials in the S region (μ_S) and Zeeman term (Γ), (a) depicted as the topological invariant and (b) low-energy eigenvalues to show the presence of zero-energy states in the trivial region. (c) Energy spectrum of the NS system with $\mu_S = 1$ meV; the gray dashed line denotes the critical Zeeman term $(\Gamma_c) = \sqrt{\mu_S + \Delta_0} = 1.118$ meV. (d) The Majorana component in the trivial region with ps-ABS and (e) MBS in the topological region.

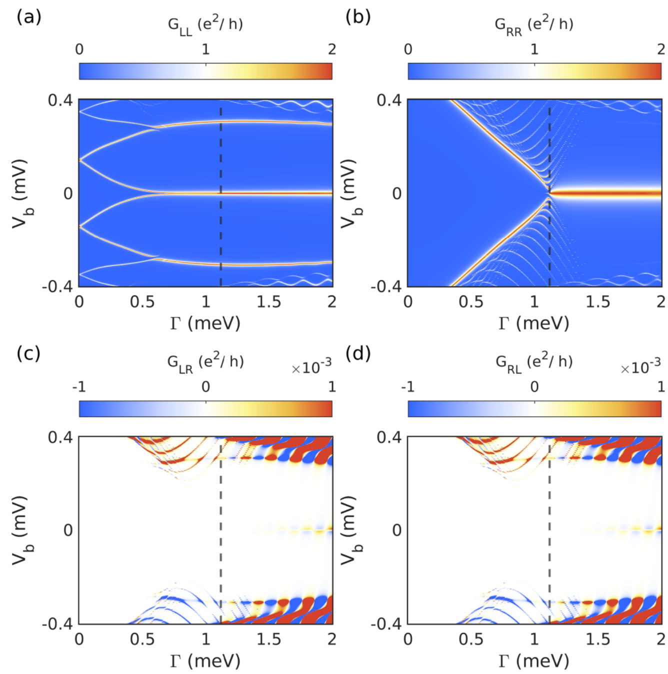

FIG. 8. NS system: [(a), (b)] Local and [(c), (d)] nonlocal conductances. Both conductances show the presence of a ZBP after Γ_c (gray dashed line) but the left conductance also shows a ZBP for the range $\Gamma < \Gamma_c$.

while for $\Gamma < \Gamma_c$ the components have significant overlap with each other and are the partially separated ABSs, as shown in Fig. 7(d).

Consider next Fig. 8, which depicts the tunneling conductance calculated for the NS heterostructure. For $\Gamma > \Gamma_c$ (denoted by the gray vertical line) both the local conductances, G_{LL} and G_{RR}, exhibit ZBPs with a peak height of $2e^2/h$ which is consistent with the presence of MBSs. It turns out that for the left lead this signature of MBSs persists even for extended values of $\Gamma < \Gamma_c$.

The trivial ZBP has a splitting at zero energy; however, the splitting is negligible, making it difficult to resolve even at low nonzero temperatures [19,30]. Another aspect which is different from the signatures in the topological regime is the absence of a ZBP on the right tunneling conductance [see Fig. 8(b)]. The reason for this is the presence of bound states only on the left side of the wire, which couples to the corresponding left lead only. The absence of correlation in the local conductance is associated with the signature of ABSs [46]. As for the nonlocal conductance, the plots in Figs. 8(c) and 8(d) exhibit too weak a signature to unambiguously distinguish the bulk gap closing at Γ_c. Similar results for the NS heterostructure have been demonstrated previously in the literature [49,50].

In this scenario where the tunneling setup involves two leads it is more likely that the inhomogeneity will be present on both sides of the nanowire. The profile used to reproduce the NSN heterostructure is given in Eq. (4) and shown in Fig. 1(b). We find that for a range of parameters the NSN structure also hosts ABSs. The same is verified from the energy spectrum in Fig. 9(a), with ABSs appearing much before the critical Zeeman term similar to that for the NS system. Even if the energy spectra for both the systems are nearly the same, the difference between the two can be seen from the Majorana component plots for the zero-energy modes as shown in Fig. 9(b). For the NSN heterostructure the bound states for $\Gamma < \Gamma_c$ are also localized at both ends just like the MBSs. These bound states are the ps-ABSs, with the partially separated Majorana components at both ends of the wire.

The tunneling conductance of the NSN heterostructure is shown in Fig. 10. Now both the left (G_{LL}) and the right

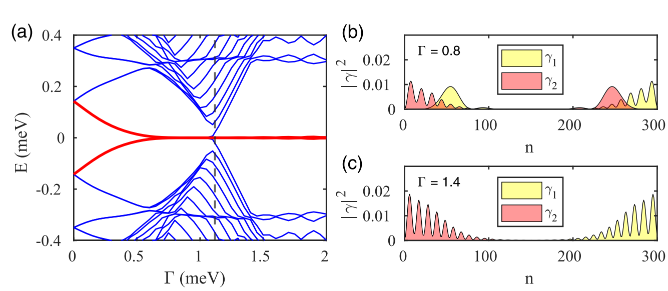

FIG. 9. NSN system with parameters $t = 25.4$ meV, $\alpha = 2$ meV, $\Delta_0 = 0.5$ meV, $N_1 = N_2 = 40$, $\mu_{N_1} = \mu_{N_2} = 0.2$ meV, $\mu_S = 1$ meV, and $N = 300$. (a) Energy spectrum with grey dashed line denoting the critical Zeeman term (Γ_c), (b) the Majorana component in the trivial region with ps-ABS, and (c) the MBS in the topological region.

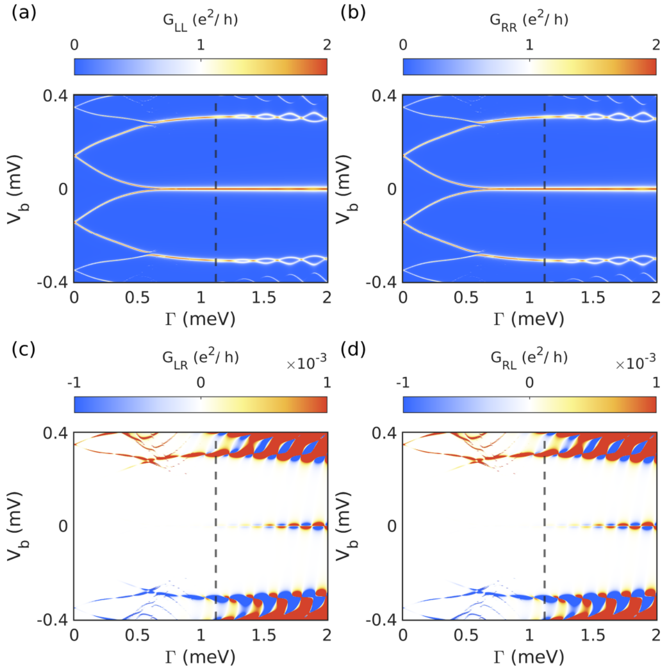

FIG. 10. NSN system: [(a), (b)] Local and [(c), (d)] nonlocal tunneling conductance. Both local conductances show a ZBP much before Γ_c (gray dashed line). Nonlocal conductance plots do not capture the band closing signature.

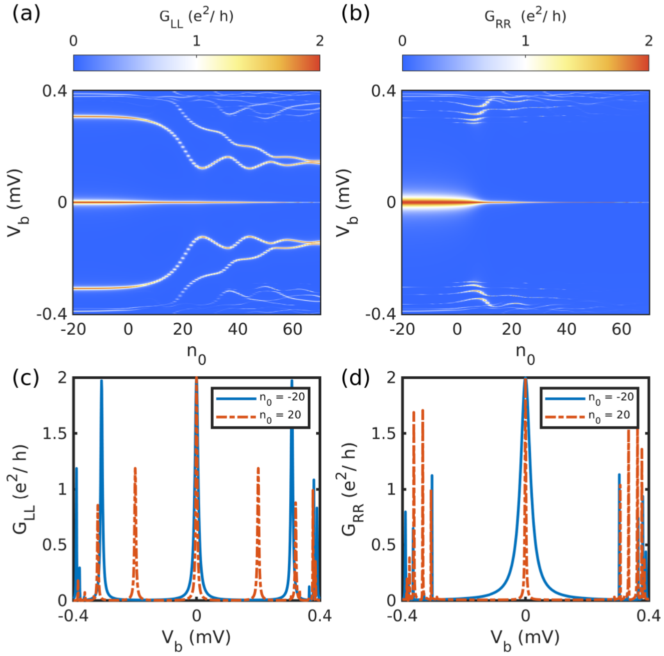

FIG. 11. NS system: Tunneling conductance signature on the application of ZMP to topological ZBP at $\Gamma > \Gamma_c$ with $\Gamma_0 = 1.4$ meV. [(a), (b)] Local tunneling conductance for a range of n_0 values and [(c), (d)] vertical line cut of the conductance for specific n_0, showing robustness of topological ZBP.

(G_{RR}) local conductances exhibit quantized ZBPs and are also correlated. As before, these signatures are present even for $\Gamma < \Gamma_c$. However, even for this system the nonlocal conductance is unable to capture the band gap closing. This can again be attributed to the bulk states being localized in the superconducting region. Thus the correlated quantized ZBP produced by the ps-ABSs and the absence of band gap signature implies no distinguishing feature between the ABS and the MBS. These conclusions were reported previously by Hess *et al.* [50].

We will now present the effect of ZMP on the trivial and topological ZBPs for the inhomogeneous system. As we saw before, the NS system has both the topological and trivial quantized ZBPs. The quantized ZBP for $\Gamma > \Gamma_c$ is present in both the left and the right local conductance, which on the application of the ZMP persists for a range of n_0 values (Fig. 11). This result is similar to the case of homogeneous wire with topological ZBP as discussed in Sec. III A. Interestingly, the effect of the ZMP on the trivial ZBP present on the left conductance for the NS system is significantly different (see Fig. 12). The ZBP splits into two separate peaks as n_0 increases. As discussed before, the topological and trivial peaks for the NSN system are the most challenging to distinguish. So we apply the ZMP to the tunneling conductance signature to the NSN system. The topological ZBP persists for an extended range of n_0, and the peak width decreases with an increase in n_0 (see Fig. 13) as is the case for the NS system. In contrast, under the ZMP, the trivial ZBP present on both local conductances splits into two separate peaks as shown in Fig. 14.

To get an insight into the behavior of topological and trivial peaks under the moving protocol, we focus our attention on the Majorana components of the state close to zero energy. Figure 15 shows the effect of the ZMP on the Majorana components of the trivial states close to zero energy for the NS system. The trivial ZBP originates due to the ps-ABS which involves partially separated Majorana components. Under the application of the ZMP, the overlap between the Majorana components increases, causing them to acquire a finite energy split, resulting in splitting of the ZBP into two peaks away from zero bias. For the case of the NSN heterostructure we have two states close to zero energy, both of which are present at either ends of the wire. These states are ps-ABSs with small overlapping Majorana components. On the application of the ZMP, the overlap increases for both the states (see Fig. 16),

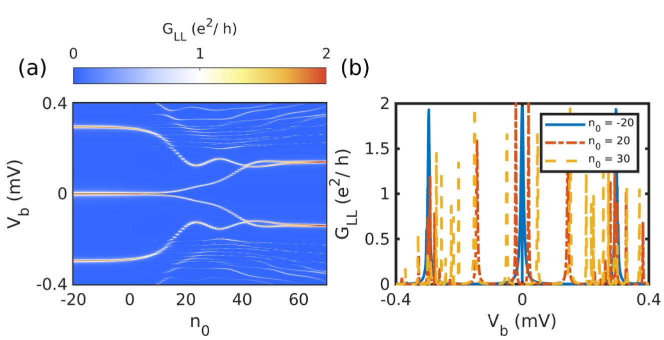

FIG. 12. NS system: Tunneling conductance signature on the application of the ZMP to trivial ZBPs at $\Gamma < \Gamma_c$ with $\Gamma_0 = 0.8$ meV. (a) Left local tunneling conductance for range of n_0 values and (b) vertical line cut of conductance for specific n_0 which captures the splitting of trivial ZBPs.

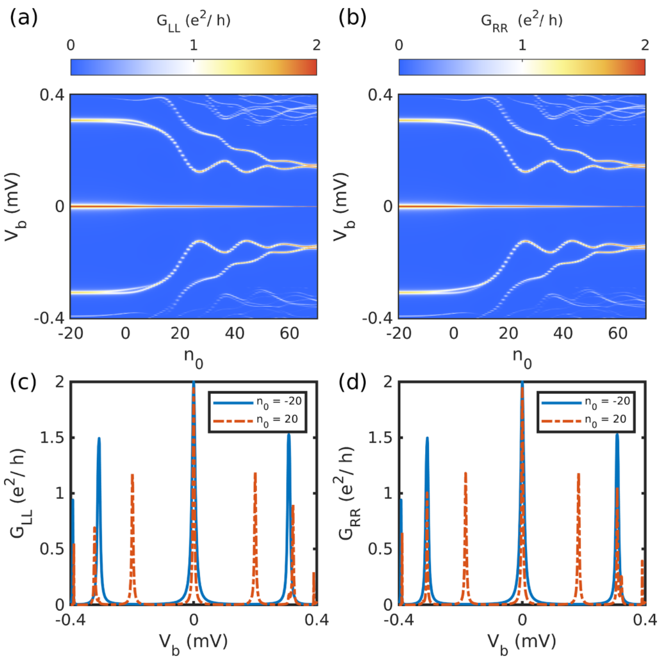

FIG. 13. NSN system: Tunneling conductance signature on the application of the ZMP to topological ZBPs at $\Gamma > \Gamma_c$ with $\Gamma_0 = 1.4$ meV. [(a), (b)] Local tunneling conductance for range of n_0 values and [(c), (d)] vertical line cut of conductance for specific n_0, capturing the robustness of topological ZBPs.

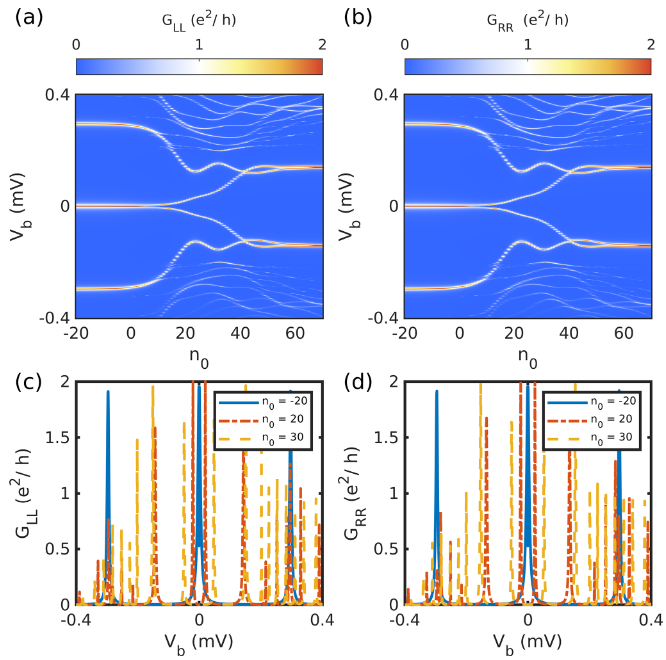

FIG. 14. NSN system: Tunneling conductance signature under the application of the ZMP to trivial ZBPs at $\Gamma < \Gamma_c$ with $\Gamma_0 = 0.8$ meV. [(a), (b)] Local tunneling conductance for range of n_0 values and [(c), (d)] vertical line cut of conductance for specific n_0, showing the splitting of trivial ZBPs in both local conductances.

resulting in a finite energy split and the trivial ZBP on both local conductances splits into two separate peaks at finite bias.

Performing similar analysis for the topological states, we show the effect of the ZMP on the Majorana components of MBSs in NS and NSN systems in Figs. 17 and 18, respectively. Fully separated Majorana components represent the MBS, and the components remain separate throughout the protocol for both the NS and NSN systems. As a result, the MBS stays at zero energy, resulting in the ZBP staying at zero bias throughout the protocol. Under the protocol, the components move away from the edge (see Fig. 18), resulting in weak coupling with the leads, leading to decreased peak width. For a large n_0 value ($\approx$70), the states will be far from the edge, making the peak disappear. Another thing to notice is that the decrease in peak height on both the local conductances of NS is different under the protocol as shown in Figs. 11(a) and 11(b). This is mainly due to the presence of the N region on the left side and MBS leaking to this region (see Fig. 18).

To showcase that the robustness of MBS energy to the ZMP and the splitting is present for all parameter ranges of ABSs, we plot the phase portrait corresponding to the lowest-energy eigenvalues for the parameter range with the ZMP for different n_0 values. As shown in Fig. 19, with $n_0 = -20$ we have a normal NSN system with low-energy ABS present before the topological region (separated by the red line); with the application of the ZMP these low-energy states move away from zero energy and for $n_0 = 40$ there are no zero-energy states outside the topological region. These plots show that the splitting is not specific to certain parameter values and the ABSs move away from zero energy for all the parameter ranges. We also like to add that the splitting we see for the trivial zero-energy state is significant and comparable to the gap present (about 70–80 % of the gap). On the other hand, the eigenvalues of the MBSs in the topological region remains unaffected.

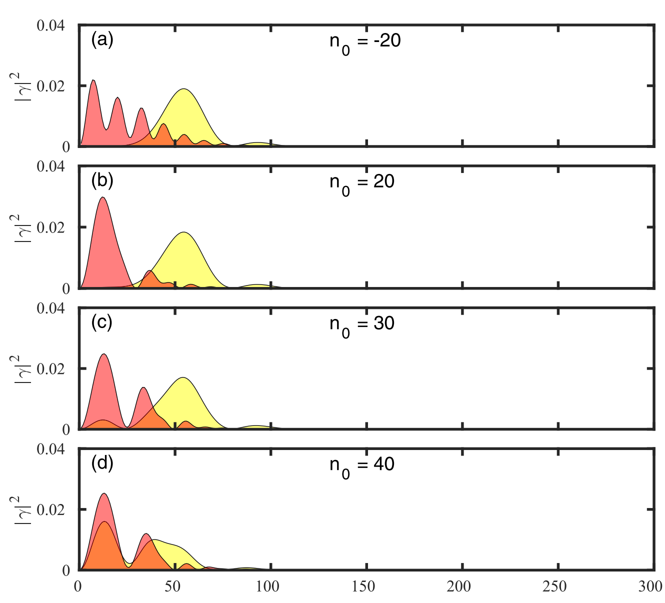

FIG. 15. Majorana components of the NS system on the application of the ZMP to the trivial state at $\Gamma < \Gamma_c$ with $\Gamma_0 = 0.8$ meV for different n_0 values. The Majorana component overlap increases with n_0.

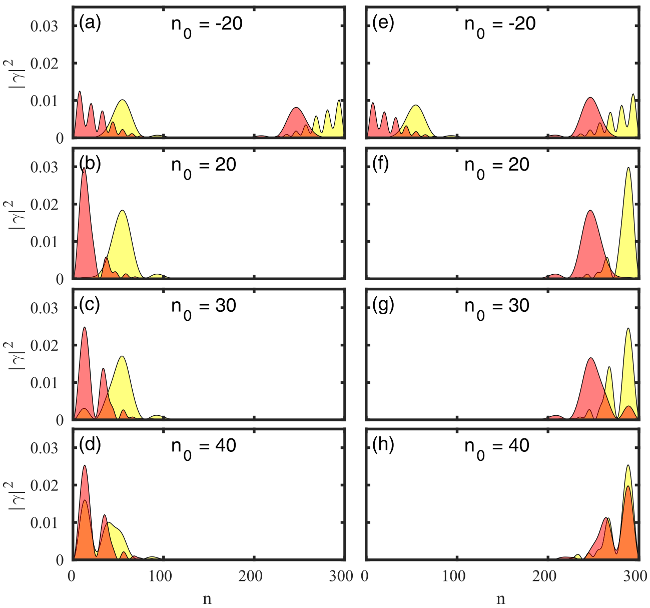

FIG. 16. Majorana components of the NSN system under the ZMP for the trivial state at $\Gamma < \Gamma_c$ with $\Gamma_0 = 0.8$ meV for different n_0 values. For both ps-ABS the overlap increases with n_0.

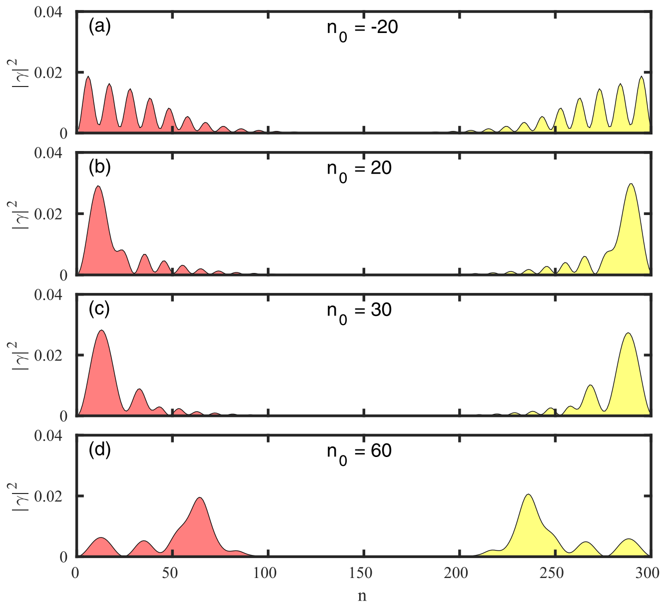

FIG. 18. Majorana components of the NSN system on the application of the ZMP to the topological state at $\Gamma > \Gamma_c$ with $\Gamma_0 = 1.4$ meV for different n_0 values. The Majorana components remain separated for a range of n_0 values.

In Appendix C we have considered the effect of the ZMP for the short nanowire scenario. We find that the energy splitting for the topological states is weakly modified while the splitting for the trivial states is large and very apparent (see Appendix C). This shows that, for the small-nanowire limit where the Majorana localization length is comparatively large, the moving protocol is able to distinguish the trivial states from the topological ones. In addition, in Appendix D we present a brief discussion on the effect of the smoothness parameter s in our moving protocol. Increasing smoothness causes the domain-wall width to increase in between the trivial and topological regions. The main results stay independent of domain-wall width unless the domain-wall width is large enough to destroy the domain structure.

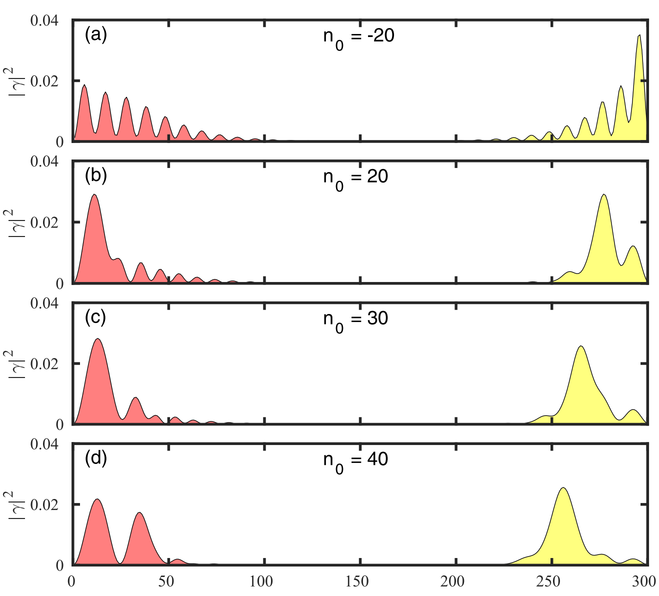

FIG. 17. Majorana components of the NS system on the application of the ZMP to the topological state at $\Gamma > \Gamma_c$ with $\Gamma_0 = 1.4$ meV for different n_0 values. Majorana components remain separated.

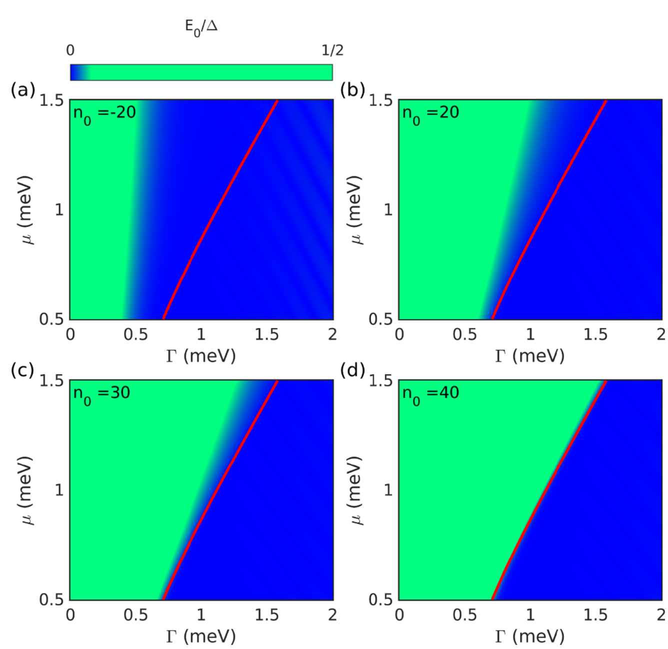

FIG. 19. Phase portrait with low-energy eigenvalues of the NSN system for a range of chemical potential (μ) in the S region and Zeeman term (Γ) with different instances of the ZMP. The ABS moves from zero energy to finite energy as n_0 is increased from (a) $n_0 = -20$ to (d) $n_0 = 40$, while the MBS in the topological regime (after red line) continues to be at zero energy.

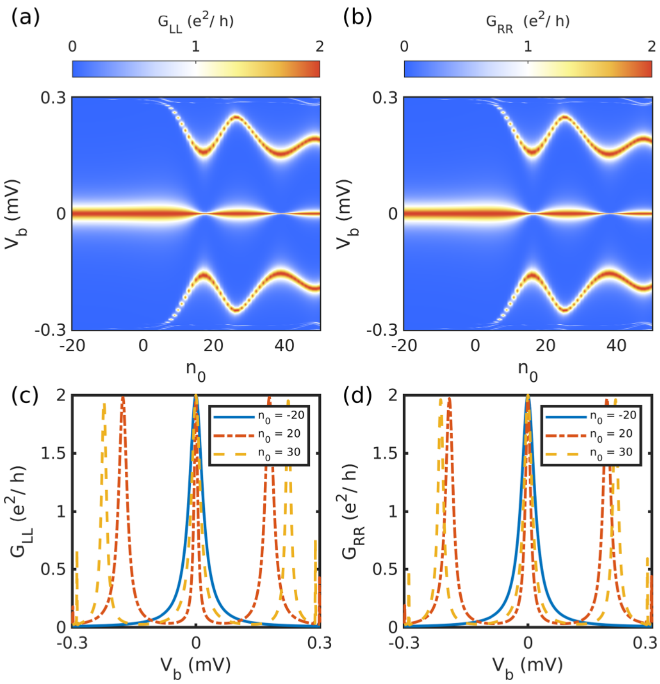

FIG. 20. Homogeneous wire tunneling conductance signature on the application of the PMP to topological ZBP at $\Gamma = 1.5$ meV $> \Gamma_c$ with $V_0 = 2$ meV. [(a), (b)] Local tunneling conductance for a range of n_0 values and [(c), (d)] vertical line cut of conductance for specific n_0, showing the robustness of topological ZBPs.

C. Moving protocol with external potential

As discussed in Sec. II, external potential can also be used to modify the topological length of a nanowire and produce a trivial-topological-trivial structure. In earlier works, this strategy has been suggested in the context of a braiding protocol [4,56–58]. However, a moving protocol with tunneling measurements at the edges has not been considered before for the purpose of distinguishing topological states from trivial ones. In this section we present the effect of the PMP on trivial and topological ZBPs.

1. Homogeneous wire

In Sec. III A, we presented the result of the ZMP on the homogeneous wire. In the case of the PMP, the behavior of topological ZBPs remains unchanged. For a range of n_0 values the topological ZBP remains robust (see Fig. 20). The most important difference between the ZMP and the one with the PMP is the MBS's confinement to the topological region. While for the PMP, the Majorana modes leak into the trivial region (see Fig. 21), it is comparatively suppressed for the ZMP. The leakage into the ends allows coupling with the lead, restoring the peak width. We find that the peak width exhibits oscillatory dependence on n_0. For example, plotted are the ZBP widths for $n_0 = 20$ and 30 in Fig. 20, and the corresponding Majorana components in Figs. 21(b) and 21(c). For $n_0 = 20$, the Majorana components are away from the lead, resulting in small peak width, while for $n_0 = 30$, the leakage of MBSs towards the ends of the wire results in an increase in peak width. While there are certain differences in the signatures corresponding to the two ways of applying the moving protocol, we would like to draw attention to the main signature corresponding to the MBS which remains unaltered for both the protocols, i.e., the peak does not move from zero bias throughout the moving protocol.

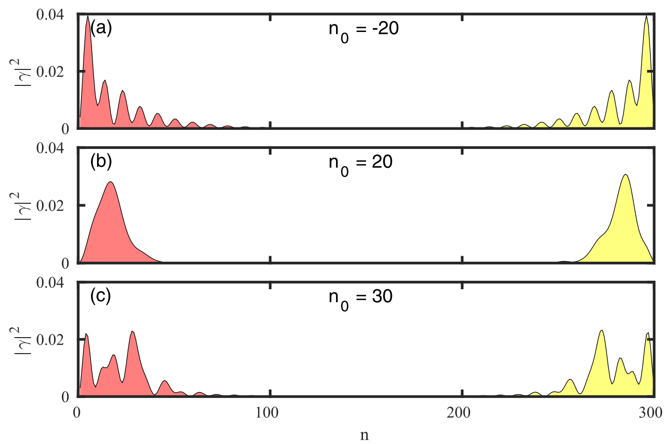

FIG. 21. Majorana components of low-energy states in homogeneous wire under the application of the PMP to topological states at $\Gamma = 1.5$ meV $> \Gamma_c$ with $V_0 = 2$ meV. Majorana components remain separated; they also leak towards the ends.

2. Inhomogeneous wire

We next consider the NSN system and study the effect of the PMP on the trivial and topological ZBPs appearing due to the inhomogeneity. As shown in Figs. 22 and 23, the main features regarding the robustness of the topological ZBP and

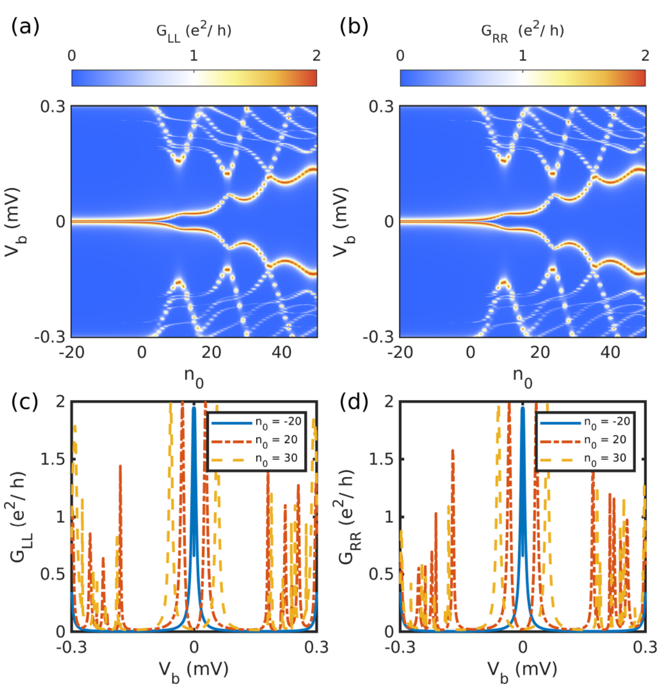

FIG. 22. NSN system: Tunneling conductance signature under the PMP to the topological ZBP at $\Gamma = 0.8$ meV $> \Gamma_c$ with $V_0 = 2$ meV. [(a), (b)] Local tunneling conductance for a range of n_0 values and [(c), (d)] vertical line cut of conductance for specific n_0; the trivial ZBP splits under the protocol.

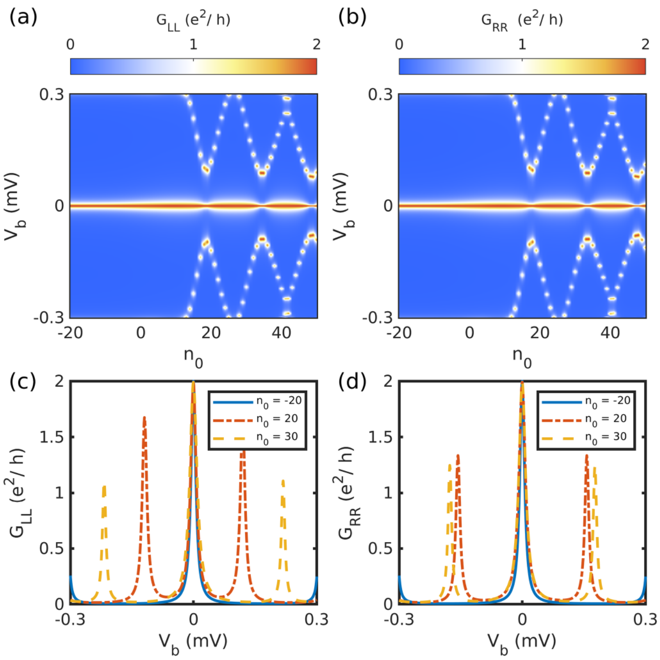

FIG. 23. NSN system: Tunneling conductance signature on the application of the PMP to the topological ZBP at $\Gamma = 1.4$ meV $> \Gamma_c$ with $V_0 = 2$ meV. [(a), (b)] Local tunneling conductance for a range of n_0 values and [(c), (d)] vertical line cut of conductance for specific n_0, showing the robustness of the topological ZBP.

the splitting of the trivial ZBP remains similar to the ZMP. As for the homogeneous case considered above, oscillations in the topological ZBP width with n_0 can be seen. This is again due to the leakage of MBSs in the ends of the wire for certain n_0 values. For topological zero-energy states Majorana components remain separated (see Fig. 24). On the other hand, for trivial zero-energy states the Majorana components exhibit an increase in overlap, resulting in the splitting of the ZBP (see Fig. 25). This result suggests the idea of a moving protocol is independent of the method used to put certain parts of the wire in a trivial regime. Both the ZMP and the PMP can be used to carry out the moving protocol, especially to distinguish topological from trivial ZBPs, based on the robustness of the ZBP.

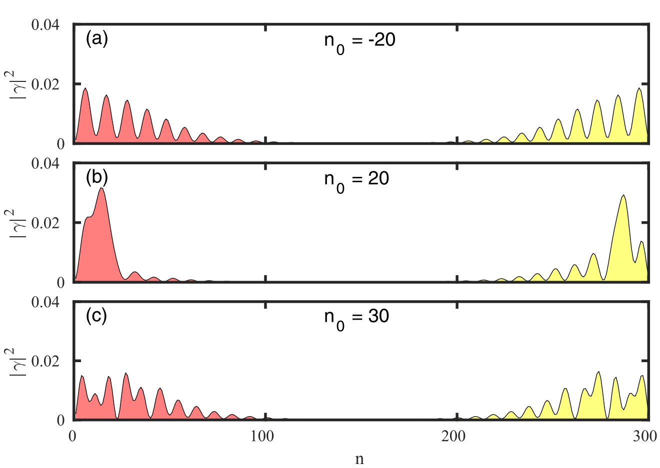

FIG. 24. Majorana components of low-energy states in the NSN system under the PMP for $\Gamma = 1.4$ meV $> \Gamma_c$ with $V_0 = 2$ meV. The components remain separated.

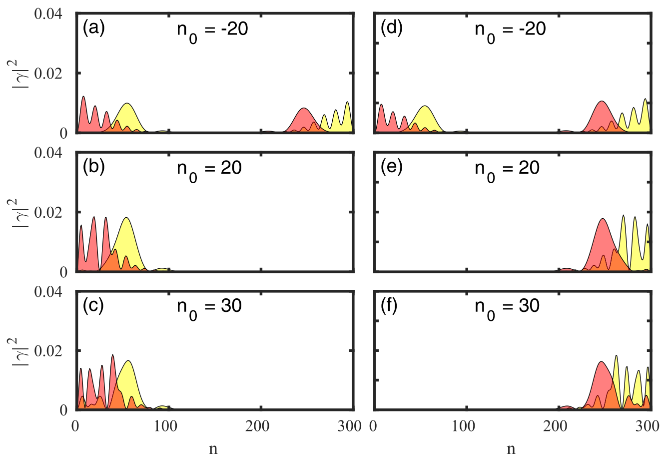

FIG. 25. Majorana components of low-energy states in the NSN system under the PMP for $\Gamma = 0.8$ meV $< \Gamma_c$ with $V_0 = 2$ meV. The Majorana component overlap increases; also they leak towards the ends.

D. S′SS′ system

In this last section we study the tunneling conductance and moving protocol results for the S′SS′ system. We utilize this system to highlight some of the shortcomings of the “moving protocol.” Nevertheless, it turns out that, compared to the Zeeman moving protocol, the potential moving protocol is partially immune to some of the shortcomings and can clearly differentiate the topological ZBP signature from the trivial ZBP signature.

On either ends of the wire, this system has zero-energy states that appear even before the critical Zeeman term ($\Gamma_c \approx \sqrt{\mu_S^2 + \Delta_0^2}$); however, as expected, the MBS emerges after the critical Zeeman term (see Fig. 26). The zero-energy states before the critical Zeeman field (Γ_c) are topological in their own right but have partially separable Majorana components; these states prior to the band gap closing are referred to as

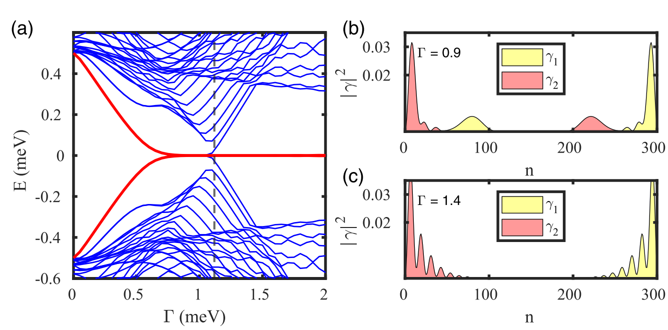

FIG. 26. S′SS′ system with parameters $t = 25.4$ meV, $\alpha = 2$ meV, $\Delta_0 = 0.5$ meV, $N_1 = N_2 = 60$, $\mu_S = 1$ meV, and $N = 300$. (a) Energy spectrum (gray dashed line denotes Γ_c). (b) Low-energy Majorana components for $\Gamma < \Gamma_c$ and (c) separated MBSs for $\Gamma > \Gamma_c$.

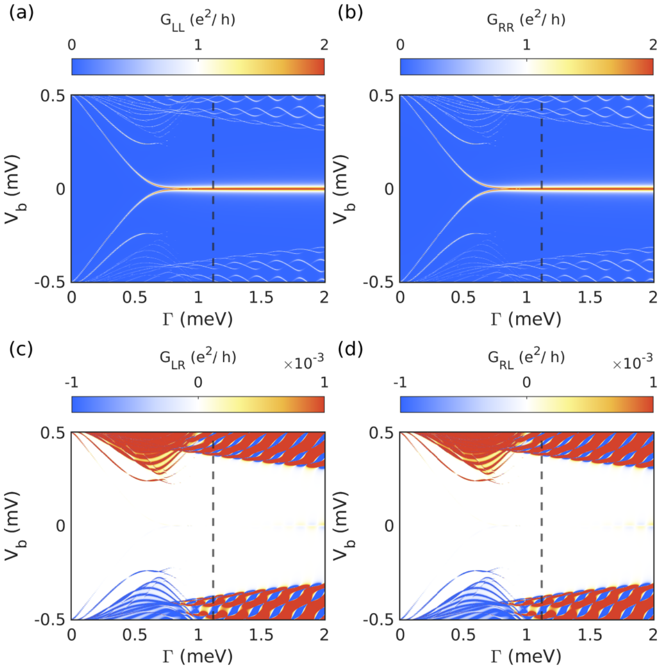

FIG. 27. S′SS′ system: [(a), (b)] Local conductance exhibits quantized ZBP in trivial and topological regions and [(c), (d)] nonlocal tunneling conductance unable to capture the band closing signature. Gray dashed line denotes Γ_c.

the quasi-MBSs [49,52]. The tunneling conductance of the system is shown in Fig. 27, where the ZBPs corresponding to both the local conductances and the nonlocal conductance fail to detect the band closing signature. We note that

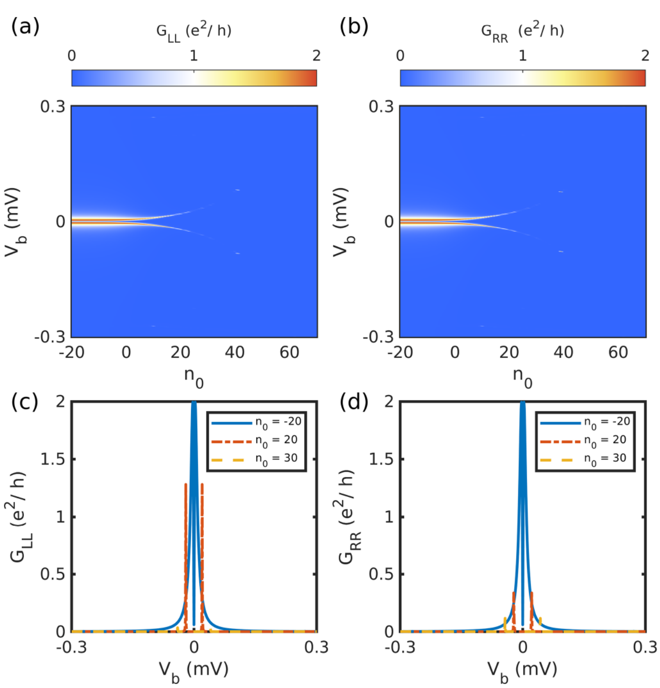

FIG. 28. S′SS′ system: Tunneling conductance signature on the application of the ZMP to the trivial ZBP at $\Gamma < \Gamma_c$ with $\Gamma_0 =$ 0.9 meV. [(a), (b)] Local tunneling conductance for a range of n_0 values and [(c), (d)] vertical line cut of conductance for specific n_0. The peak split is moderately pronounced.

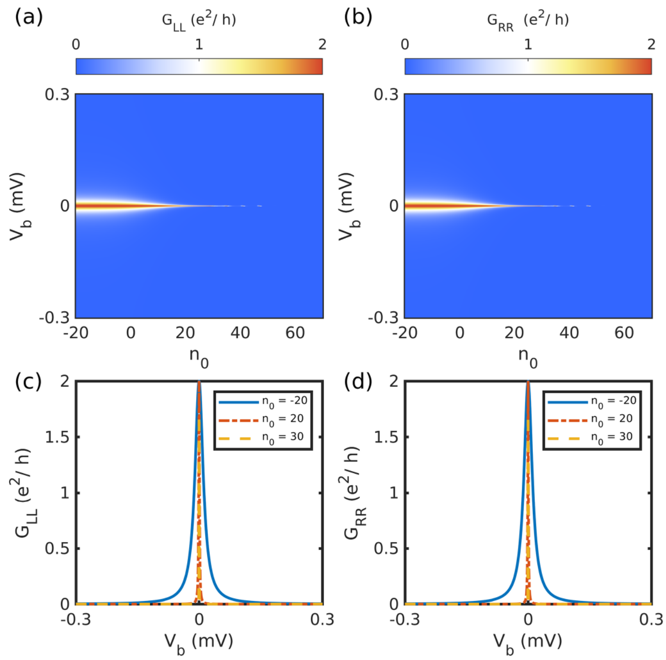

FIG. 29. S′SS′ system: Tunneling conductance signature on the application of the ZMP to the topological ZBP at $\Gamma > \Gamma_c$ with $\Gamma_0 =$ 1.4 meV. [(a), (b)] Local tunneling conductance for a range of n_0 values and [(c), (d)] vertical line cut of conductance for specific n_0. The peak remains robust before disappearing for higher n_0.

this system's tunneling conductance signatures are similar to that of the NSN system. Consequently one cannot rely only on the tunneling signature to distinguish the trivial and the topological ZBPs. Figures 28 and 29 demonstrate how the ZMP affects trivial and topological ZBPs, respectively. Here, the trivial ZBP peak splitting is only moderately noticeable. The peak splits, but before the split in the peak is pronounced, the peak height drops and disappears. On the other hand, for the topological ZBP, the conductance peak is fixed to zero bias for a range of n_0 before it too vanishes. We plot the Majorana component for low-energy states belonging to the trivial (Fig. 30) and topological (Fig. 31) regimes to determine why this is the case for various n_0 values. For trivial zero-energy states, the overlap increases with the increase in n_0, leading to a rise in the energy split. Additionally, the states drift away from the lead, weakening the coupling between the lead and the states. As a result, the peak vanishes long before the peak split can be seen clearly. Figure 31 for the topological regime with the MBS demonstrates the presence of the exact shifting of Majorana components away from the lead, which accounts for the decreased peak width and the peak's disappearance for higher n_0 values as depicted in Fig. 29.

This shortcoming of the ZMP is mainly due to the reliance on the local probes to pick the energy split signature. The protocol moves the states away from the lead, which causes the signature to disappear. As we demonstrate in Sec. III C, the PMP is immune to this effect because of the leakage of states towards the ends of the wire, retaining the coupling to the lead. For trivial and topological ZBPs, we show the results corresponding to the PMP on the S′SS′ system in Figs. 32 and 33, respectively. Figure 32 clearly illustrates the trivial ZBP

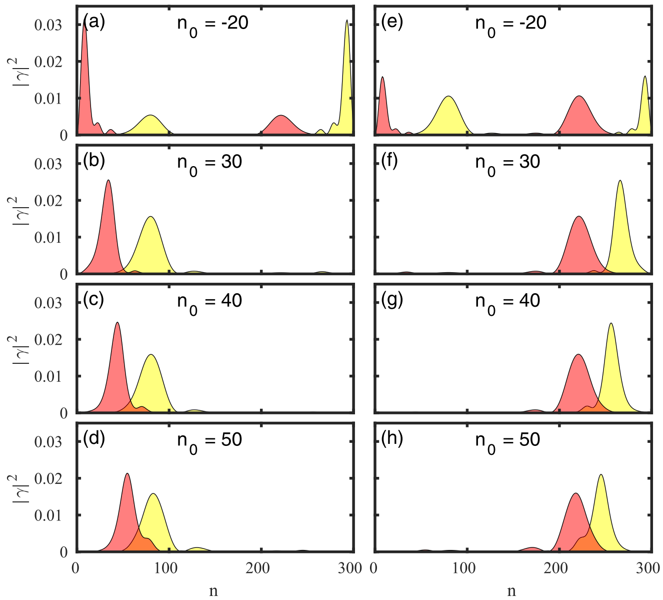

FIG. 30. Majorana components of the S′SS′ system on the application of the ZMP to the trivial state at $\Gamma < \Gamma_c$ with $\Gamma_0 = 0.9$ meV for different n_0 values, showing increase in the overlap and the components moving away from the ends.

splitting during the moving protocol. As shown in Fig. 34, the states leak towards the ends, thereby improving the split visibility. From the tunneling conductance plot in Fig. 33 and the analogous Majorana component plot in Fig. 35, it is clear that the resilience of the topological ZBP is also present for this scenario. We want to stress the fact that both moving protocols can induce energy splitting in trivial zero-energy states, but as we use a local tunneling conductance probe to detect this splitting the PMP is better at capturing the split as well as the robustness in the ZBP.

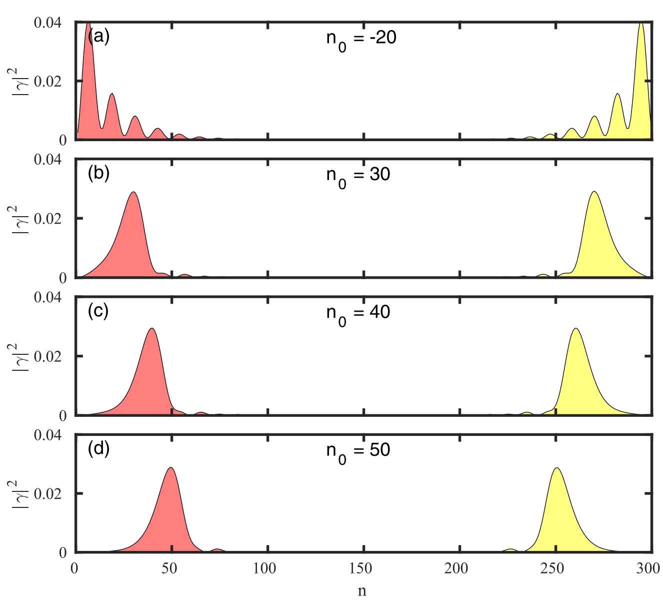

FIG. 31. Majorana components of the S′SS′ system on the application of the ZMP to the topological state at $\Gamma > \Gamma_c$ with $\Gamma_0 = 1.4$ meV for different n_0 values, showing the components moving away from the edge while being separated.

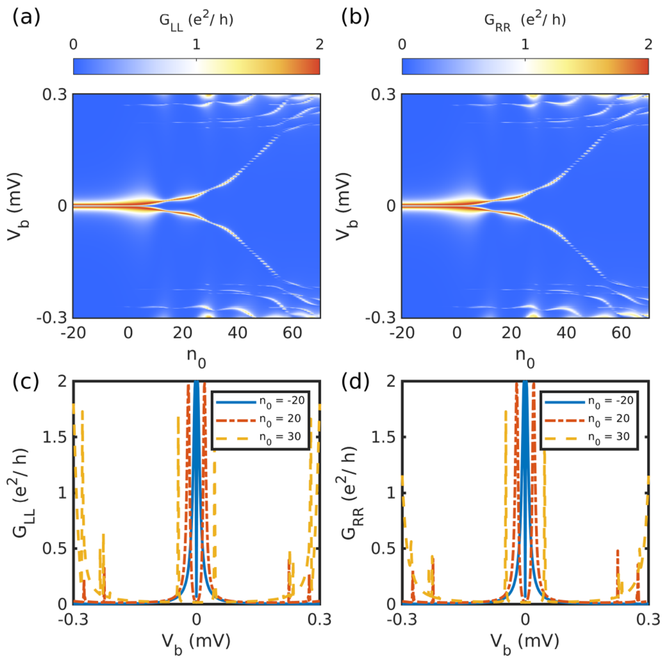

FIG. 32. S′SS′ system: Tunneling conductance signature on the application of the PMP to the trivial ZBP at $\Gamma = 0.9$ meV $< \Gamma_c$ with $V_0 = 2$ meV. [(a), (b)] Local tunneling conductance for a range of n_0 values and [(c), (d)] vertical line cut of conductance for specific n_0, capturing the splitting signatures.

IV. CONCLUSION

In this article, we have reproduced the tunneling conductance signatures from heterostructures and have verified the inability of local and nonlocal conductance to distinguish ABSs from MBSs. Since both the trivial and nontrivial zero-energy states produce a quantized ZBP in local conductance, we focus on the effects of the topological length of the nanowire on the ZBP. We show that by applying the moving protocol, the trivial and topological ZBPs behave differently. As the Majorana components of trivial and topological states are fundamentally different, the protocol affects them differently. For MBSs, the Majorana components are entirely separated and localized at the edges of the topological region. The Majorana components move away from the wire's edges when the protocol is applied; however, they remain separated and are therefore pinned at zero energy, causing the peak in local conductance to remain at zero bias throughout the protocol. For trivial zero-energy states when the protocol is applied, the overlap between the partially separated Majorana components increases, causing the trivial states to move away from zero energy. As a result, the trivial ZBP splits into two peaks. This effect of the moving protocol on topological and trivial ZBPs remains the same irrespective of the method of reducing the topological length by putting a certain portion of the wire in a trivial regime. We compare the results of ZBPs under the ZMP and the PMP in our numerical simulation. We discuss the shortcoming of the moving protocol in the S′SS′

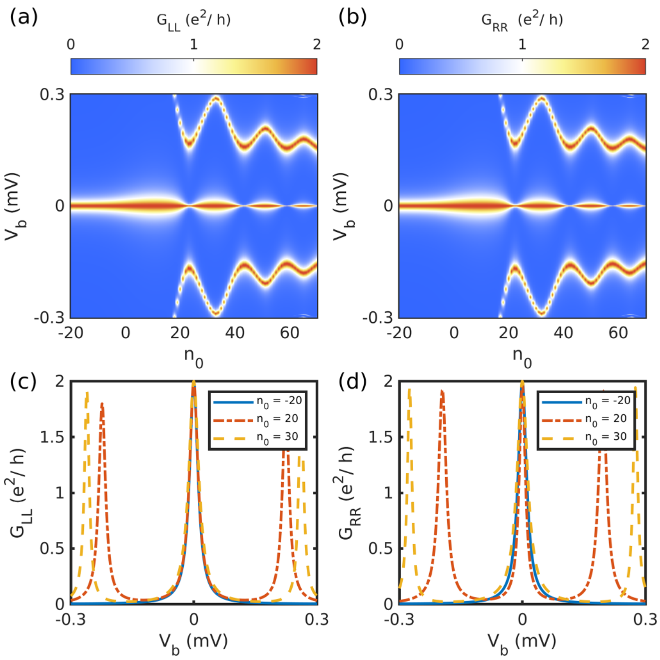

FIG. 33. S′SS′ system: Tunneling conductance signature on the application of the PMP to the topological ZBP at $\Gamma = 1.4$ meV $> \Gamma_c$ with $V_0 = 2$ meV. [(a), (b)] Local tunneling conductance for a range of n_0 values and [(c), (d)] vertical line cut of conductance for specific n_0, showing the robustness of the topological ZBP.

system, the origin of which is due to the reliance on the local measurements to detect the split in energy. As the states are moved farther away from the lead, the splitting information is less pronounced in tunneling conductance. However, for PMP, the leakage of the states towards the ends preserves the coupling to the leads, making the protocol immune to this vulnerability.

In the literature, many proposals have been suggested to create and move domain walls specific to the experimental setup and geometry. Some of these involve altering the gate voltage [56] or magnetic field gradient [61], the

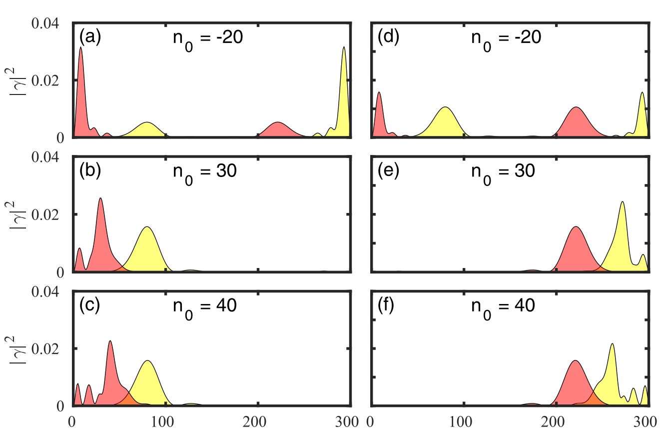

FIG. 34. Majorana components of low-energy states in the S′SS′ system under the PMP for $\Gamma = 0.9$ meV $< \Gamma_c$ with $V_0 = 2$ meV, denoting the overlap increasing as well as states leaking towards the ends.

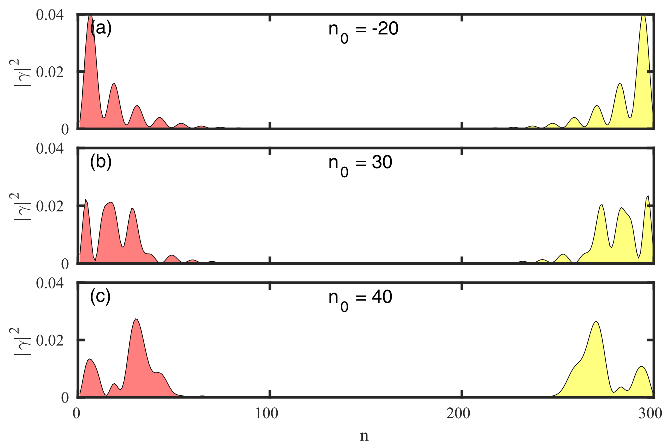

FIG. 35. Majorana components of low-energy states in the S′SS′ system under the PMP at $\Gamma = 1.4$ meV $> \Gamma_c$ with $V_0 = 2$ meV, showing separated components.

use of gate-tunable valves [62], the application of external magnetic fields in the presence of spin-orbit coupling and helimagnetic order [63], or the control of the magnetic texture within two-dimensional electron gases [64]. Nanowires in proximity to amplitude-modulated magnetic textures can in principle be used to create the domain wall and with the help of spintronic technology the magnetic texture can be controlled to move the domain wall [61,65]. The experimental difficulties vary from model to model; for example, in semiconductor-superconductor nanowires, the gate voltage controls the chemical potential, and increasing the gate voltage causes the electron density to increase, which will in turn affect the g factor, causing the Zeeman term to change. In this case, one needs to find an effective gate voltage to put the ends in a trivial region and control it locally using a keyboard layout to move the domain wall. The local control of parameters is needed to implement the moving protocol, and fabricating such sophisticated heterostructures to achieve it remains a daunting challenge. Regardless, moving and controlling the Majorana modes localized between the topological and trivial domains is a necessity for the realization of topological qubits. With the improvement in fabrication technology and experimental control, the implementation of the moving protocol to differentiate topological states from the trivial ones and controlling Majorana modes can be realized. Recent works in nanoscale magnetic field [66], spintronics [67], and ferromagnets [68,69] hold promise for the realization of the moving protocol in real experimental settings.

To summarize, we have demonstrated through our numerical studies that the moving protocol combined with the tunneling conductance allows one to probe the Majorana component signatures and distinguish topological states from the trivial ones. This different response of ZBPs under the moving protocol if realized can distinguish trivial ZBPs from the topological ones.

ACKNOWLEDGMENTS

D.S. would like to thank CSIR for funding by their File No. 09/1020(0216)/2021-EMR-I. S.G. is grateful to the SERB, Government of India, for the support via the Core Research Grant No. CRG/2020/002731. We also thank J. Carlos Egues and Poliana H. Penteado for the fruitful discussion.

APPENDIX A: CALCULATION OF TOPOLOGICAL QUANTUM NUMBER

1. Scattering matrix method

To calculate the topological quantum number, we briefly discuss the scattering matrix method here [59]. A scattering matrix characterizes a linear relation between the outgoing wave amplitudes and the incoming wave amplitudes at each energy:

$$\begin{pmatrix} c_l^o \\ c_r^o \end{pmatrix} = S(E)\begin{pmatrix} c_l^i \\ c_r^i \end{pmatrix}. \tag{A1}$$

The superscript i (o) is for amplitudes of the waves moving towards (from) the scatterer and the subscript l (r) is for waves on the left (right) of the scatterer. We can express the scattering matrix in terms of transmission and reflection amplitudes in the following form:

$$S = \begin{pmatrix} r & t' \\ t & r' \end{pmatrix}. \tag{A2}$$

Here, $\{t, t'\}$ ($\{r, r'\}$) represent the 4×4 transmission (reflection) matrices. The transfer matrix relates the wave amplitudes on the right-hand side to the left-hand side of the sample:

$$\begin{pmatrix} c_r^o \\ c_r^i \end{pmatrix} = M\begin{pmatrix} c_l^o \\ c_l^i \end{pmatrix}. \tag{A3}$$

From Eqs. (A1) and (A3), one can express the elements of the transfer matrix in terms of the elements of the scattering matrix as follows:

$$M = \begin{pmatrix} M_{11} & M_{12} \\ M_{21} & M_{22} \end{pmatrix} = \begin{pmatrix} t - r't'^{-1}r & r't'^{-1} \\ -t'^{-1}r & t'^{-1} \end{pmatrix}. \tag{A4}$$

Analogous to Eq. (A4), we can also decompose the scattering matrix in terms of the elements of the transfer matrix as follows:

$$S = \begin{pmatrix} r & t' \\ t & r' \end{pmatrix} = \begin{pmatrix} -M_{22}^{-1}M_{21} & M_{22}^{-1} \\ M_{11} - M_{12}M_{22}^{-1}M_{21} & M_{12}M_{22}^{-1} \end{pmatrix}. \tag{A5}$$

The conservation of the probability current also introduces a relationship between the elements of the transfer matrix M [70]:

$$M^\dagger \Sigma_z M = \Sigma_z, \quad \Sigma_z = \begin{pmatrix} \mathbb{I} & 0 \\ 0 & -\mathbb{I} \end{pmatrix}. \tag{A6}$$

From the definition of the transfer matrix it is clear that it obeys the multiplicative composition law,

$$M = M_2 M_1. \tag{A7}$$

This composition law for transfer matrices results in a nonlinear composition of scattering matrices. Using Eqs. (A4) and (A7), we obtain

$$\begin{aligned} M &= \begin{pmatrix} t - r't'^{-1}r & r't'^{-1} \\ -t'^{-1}r & t'^{-1} \end{pmatrix} \\ &= \begin{pmatrix} t_2 - r_2't_2'^{-1}r_2 & r_2't_2'^{-1} \\ -t_2'^{-1}r_2 & t_2'^{-1} \end{pmatrix}\begin{pmatrix} t_1 - r_1't_1'^{-1}r_1 & r_1't_1'^{-1} \\ -t_1'^{-1}r_1 & t_1'^{-1} \end{pmatrix}. \end{aligned} \tag{A8}$$

This gives the composite S matrix of the system [70]:

$$\begin{aligned} S &= \begin{pmatrix} r & t' \\ t & r' \end{pmatrix} \\ &= \begin{pmatrix} r_1 + t_1'(\mathbb{I} - r_2r_1')^{-1}r_2t_1 & t_1'(\mathbb{I} - r_2r_1')^{-1}t_2' \\ t_2(\mathbb{I} - r_1'r_2)^{-1}t_1 & r_2' + t_2(\mathbb{I} - r_1'r_2)^{-1}r_1't_2' \end{pmatrix}. \end{aligned} \tag{A9}$$

The composition law, Eq. (A9), for scattering matrices is denoted by

$$S = S_2 \otimes S_1. \tag{A10}$$

2. Topological quantum number

The Hamiltonian in Eq. (1) can be rewritten in the Bogoliubov–de Gennes (BdG) basis $\Psi_n = (c_{n\uparrow}, c_{n\downarrow}, c_{n\downarrow}^\dagger, -c_{n\uparrow}^\dagger)^T$:

$$H_{\text{BdG}} = \frac{1}{2}\sum_n [\Psi_n^\dagger \hat{h}_n \Psi_n + (\Psi_n^\dagger \hat{t}_n \Psi_{n+1} + \text{H.c.})]. \tag{A11}$$

Writing the zero-energy Schrödinger equation for the BdG Hamiltonian in Eq. (A11) gives us a recursive relation between two sites in terms of the transfer matrix $\mathcal{M}_n$ [59,71]:

$$\mathcal{M}_n = \begin{pmatrix} 0 & \hat{t}_n^\dagger \\ -\hat{t}_n^{-1} & -\hat{t}_n^{-1}\hat{h}_n \end{pmatrix}. \tag{A12}$$

Now, $\mathcal{M}_n$ gives the relation between the two nearest-neighbor sites, but it is different from the definition used in Eq. (A3). The probability current conservation is given by [71]

$$\mathcal{M}_n^\dagger \Sigma_y \mathcal{M}_n = \Sigma_y, \quad \Sigma_y = \begin{pmatrix} 0 & -i\mathbb{I} \\ i\mathbb{I} & 0 \end{pmatrix}. \tag{A13}$$

Therefore, we transform to the new basis using a unitary transformation:

$$M_n = \mathcal{U}^\dagger \mathcal{M}_n \mathcal{U}, \quad \mathcal{U} = \frac{1}{\sqrt{2}}\begin{pmatrix} \mathbb{I} & \mathbb{I} \\ i\mathbb{I} & -i\mathbb{I} \end{pmatrix}. \tag{A14}$$

In this basis, the transfer matrix M_n now satisfies Eq. (A6). As a result, all of the properties of the transfer matrix outlined in Sec. A 1 apply to this transfer matrix. Thus, using Eq. (A5), we construct the unitary scattering matrix at each site and then, using the composition law [Eq. (A9)], we obtain the composite scattering matrix of the N-dot chain:

$$S = \begin{pmatrix} R & T' \\ T & R' \end{pmatrix} = S_N \otimes S_{N-1} \otimes \cdots \otimes S_1. \tag{A15}$$

The topological quantum number TI is given by [72,73]

$$\text{TI} = \text{sgn}[\text{Det}(R)], \tag{A16}$$

where r is the subblock of the total scattering matrix S [Eq. (A2)] of the chain at Fermi level. The Majorana bound states exist at the end points of the chain if TI $= -1$. This phase is the topologically nontrivial phase. On the other hand, a value of TI $= +1$ means that the system is in the trivial phase.

APPENDIX B: TUNNELING CONDUCTANCE

The expression of tunneling conductance in terms of the scattering matrix is well known in the literature [74,75] and is given by

$$G_{\rm LL} = \frac{e^2}{h}\int_{-\infty}^{\infty} d\omega\left[-\frac{dn_L(\omega)}{d(eV_L)}\right]\Big\{{\rm Tr}\Big[2r_{eh}^{\rm LL}\big(r_{eh}^{\rm LL}\big)^\dagger + t_{ee}^{\rm LR}\big(t_{ee}^{\rm LR}\big)^\dagger + t_{eh}^{\rm LR}\big(t_{eh}^{\rm LR}\big)^\dagger\Big]\Big\}_\omega, \tag{B1}$$

$$G_{\rm LR} = \frac{e^2}{h}\int_{-\infty}^{\infty} d\omega\left[\frac{dn_R(\omega)}{d(eV_R)}\right]\Big\{\Big[t_{ee}^{\rm LR}\big(t_{ee}^{\rm LR}\big)^\dagger - t_{eh}^{\rm LR}\big(t_{eh}^{\rm LR}\big)^\dagger\Big]\Big\}_\omega, \tag{B2}$$

$$G_{\rm RL} = \frac{e^2}{h}\int_{-\infty}^{\infty} d\omega\left[\frac{dn_L(\omega)}{d(eV_L)}\right]\Big\{\Big[t_{ee}^{\rm RL}\big(t_{ee}^{\rm RL}\big)^\dagger - t_{eh}^{\rm RL}\big(t_{eh}^{\rm RL}\big)^\dagger\Big]\Big\}_\omega, \tag{B3}$$

$$G_{\rm RR} = \frac{e^2}{h}\int_{-\infty}^{\infty} d\omega\left[-\frac{dn_R(\omega)}{d(eV_R)}\right]\Big\{{\rm Tr}\Big[2r_{eh}^{\rm RR}\big(r_{eh}^{\rm RR}\big)^\dagger + t_{ee}^{\rm RL}\big(t_{ee}^{\rm RL}\big)^\dagger + t_{eh}^{\rm RL}\big(t_{eh}^{\rm RL}\big)^\dagger\Big]\Big\}_\omega, \tag{B4}$$

where $n_\alpha(\omega) = n_F(\omega + eV_\alpha)$ is the Fermi function at the α lead with α being L or R. The derivative of the Fermi function becomes the Dirac delta function at 0 K temperature leading to the simple equations

$$G_{\rm LL} = \frac{e^2}{h}\Big\{{\rm Tr}\Big[2r_{eh}^{\rm LL}\big(r_{eh}^{\rm LL}\big)^\dagger + t_{ee}^{\rm LR}\big(t_{ee}^{\rm LR}\big)^\dagger + t_{eh}^{\rm LR}\big(t_{eh}^{\rm LR}\big)^\dagger\Big]\Big\}_{\omega=eV_L}, \tag{B5}$$

$$G_{\rm LR} = -\frac{e^2}{h}\Big\{\Big[t_{ee}^{\rm LR}\big(t_{ee}^{\rm LR}\big)^\dagger - t_{eh}^{\rm LR}\big(t_{eh}^{\rm LR}\big)^\dagger\Big]\Big\}_{\omega=eV_R}, \tag{B6}$$

$$G_{\rm RL} = -\frac{e^2}{h}\Big\{\Big[t_{ee}^{\rm RL}\big(t_{ee}^{\rm RL}\big)^\dagger - t_{eh}^{\rm RL}\big(t_{eh}^{\rm RL}\big)^\dagger\Big]\Big\}_{\omega=eV_L}, \tag{B7}$$

$$G_{\rm RR} = \frac{e^2}{h}\Big\{{\rm Tr}\Big[2r_{eh}^{\rm RR}\big(r_{eh}^{\rm RR}\big)^\dagger + t_{ee}^{\rm RL}\big(t_{ee}^{\rm RL}\big)^\dagger + t_{eh}^{\rm RL}\big(t_{eh}^{\rm RL}\big)^\dagger\Big]\Big\}_{\omega=eV_R}. \tag{B8}$$

We use a Green's function formalism to calculate the scattering matrices needed for conductance. The retarded Green's function for the system connected to two leads is given by

$$G^r(\omega) = \frac{1}{(\omega + i\eta)I - H_{\rm BdG} - \Sigma_L^r - \Sigma_R^r} \tag{B9}$$

where I is an identity matrix and Σ_α^r denotes the self-energy due to the α lead. Under the broadband approximation the self-energy can be written in terms of a level broadening matrix as $\Sigma_\alpha^r = -i\Gamma_\alpha/2$. The broadening matrix is diagonal, taking the form $\Gamma_\alpha = \gamma_\alpha I$. The broadening γ_α is treated as a parameter in the numerics [75], to calculate the retarded Green's function which we fix to $\gamma_\alpha = 0.2t$ for all our calculations. It effectively describes the coupling of the nanowire with the conductance lead; for small values of γ_α our result also holds. The BdG Hamiltonian is written in the Nambu basis and the Green's function has the form

$$G_{i,j}^r(\omega) = \begin{pmatrix} g_{i,j}^r(\omega) & f_{i,j}^r(\omega) \\ \bar{f}_{i,j}^r(\omega) & \bar{g}_{i,j}^r(\omega) \end{pmatrix}. \tag{B10}$$

With this particular form for the Green's function we could define the scattering matrix elements as

$$r_{ee}^{\rm LL} = \gamma_L g_{1,1}^r, \qquad r_{ee}^{\rm RR} = \gamma_R g_{N,N}^r, \tag{B11}$$

$$r_{eh}^{\rm LL} = \gamma_L f_{1,1}^r, \qquad r_{ee}^{\rm RR} = \gamma_R f_{N,N}^r, \tag{B12}$$

$$t_{ee}^{\rm LR} = \sqrt{\gamma_L\gamma_R}\, g_{1,N}^r, \qquad t_{eh}^{\rm LR} = \sqrt{\gamma_L\gamma_R}\, f_{1,N}^r, \tag{B13}$$

$$t_{ee}^{\rm RL} = \sqrt{\gamma_L\gamma_R}\, g_{N,1}^r, \qquad t_{eh}^{\rm RL} = \sqrt{\gamma_L\gamma_R}\, f_{N,1}^r. \tag{B14}$$

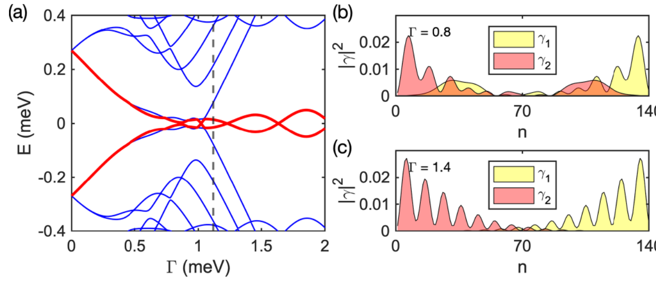

FIG. 36. NSN system with parameters $t = 25.4$ meV, $\alpha = 2$ meV, $\Delta_0 = 0.5$ meV, $N_1 = N_2 = 20$, $\mu_{N_1} = \mu_{N_2} = 0.2$ meV, $\mu_S = 1$ meV, and $N = 140$. (a) Energy spectrum with grey dashed line denoting the critical Zeeman term (Γ_c), (b) the Majorana component in the trivial region with ps-ABS, and (c) the MBS in the topological region.

APPENDIX C: SMALL NANOWIRE SCENARIO

In this section, we consider the NSN system in the small-nanowire limit where the Majorana localization length is nearly half of the length of the nanowire. The energy spectrum shown in Fig. 36 shows the presence of trivial and topological in-gap states (in this limit, their energy split is also clearly visible).

The tunneling conductance for this system is shown in Fig. 37. The local conductance captures the Majorana oscillations, and before Γ_c it also exhibits conductance peaks from the trivial in-gap state. We apply the ZMP on the conductance peaks present in trivial and topological regimes, the results of which are shown in Figs. 38 and 39, respectively. As expected, due to the partial overlap of the trivial in-gap states they acquire a large energy split under the protocol, causing the peaks to move towards the high bias voltage (see Fig. 38). While for topological in-gap states, the already present Majorana oscillation stays in the same range, and the energy split appears to decrease a little. For topological states, the Majorana component plot is shown in Fig. 40, which clearly shows the components remaining nearly separated under the moving protocol. It is interesting to note that even in this small-length limit of nanowires, the effect of the moving protocol provides a distinguishing signature in our numerical analysis. However,

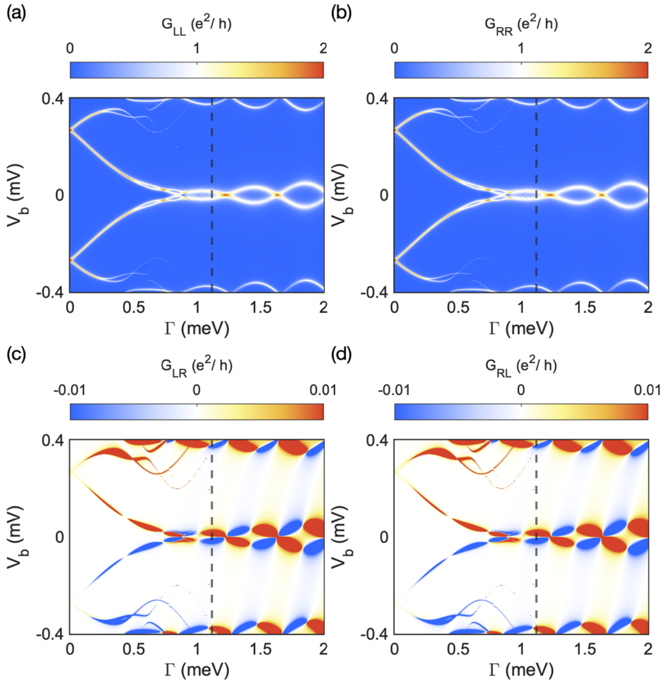

FIG. 37. NSN system: [(a), (b)] Local and [(c), (d)] nonlocal tunneling conductance. Both local conductances shows peaks close to zero bias before and after Γ_c (gray dashed line). Nonlocal conductance plots do not capture the band closing signature.

it is important to acknowledge that the moving protocol may not be suitable for very small nanowires characterized by significant Majorana component overlap.

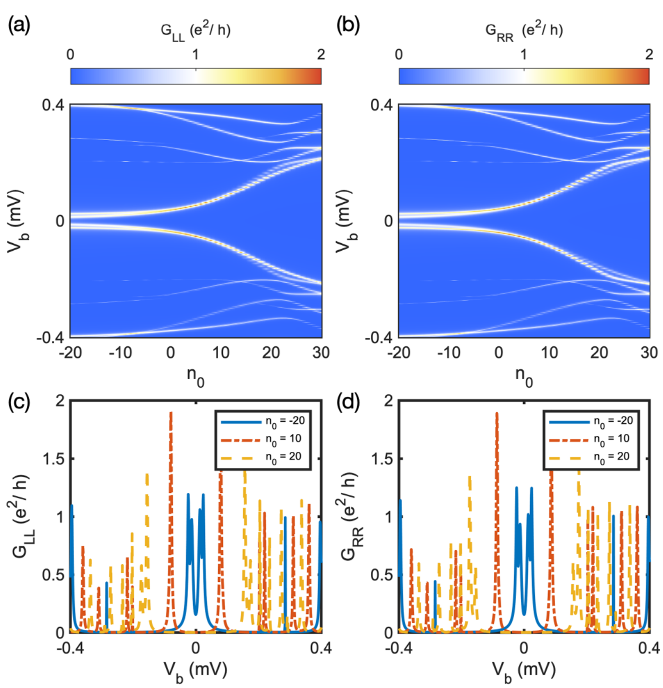

FIG. 38. NSN system: Tunneling conductance signature under the application of the ZMP to trivial conductance peaks at $\Gamma < \Gamma_c$ with $\Gamma_0 = 0.8$ meV. [(a), (b)] Local tunneling conductance for range of n_0 values and [(c), (d)] vertical line cut of the conductance for specific n_0, showing the energy splitting to increase for trivial states.

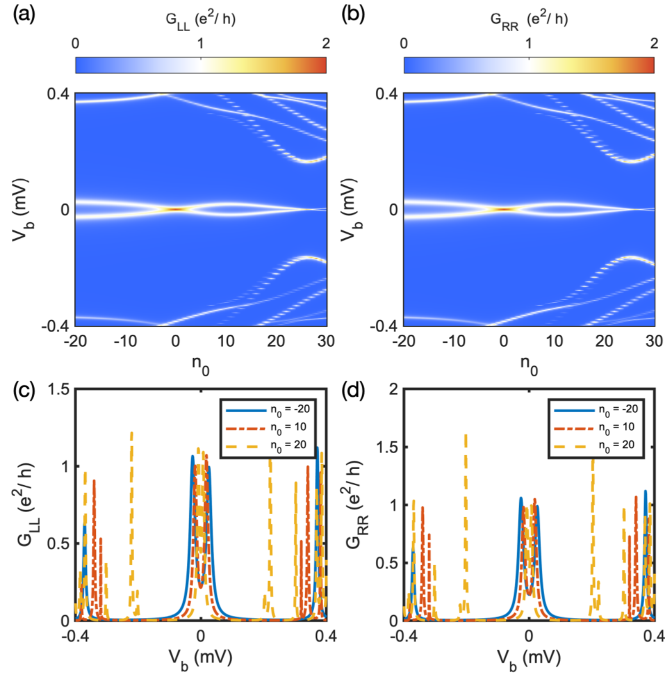

FIG. 39. NSN system: Tunneling conductance signature on the application of the ZMP to topological conductance peaks at $\Gamma > \Gamma_c$ with $\Gamma_0 = 1.4$ meV. [(a), (b)] Local tunneling conductance for range of n_0 values and [(c), (d)] vertical line cut of the conductance for specific n_0, capturing the energy split to remain in the same range but not increase.

APPENDIX D: EFFECT OF SMOOTHNESS PARAMETER

In this section, we study the effect of the smoothness parameter (s), which controls the domain-wall width in our

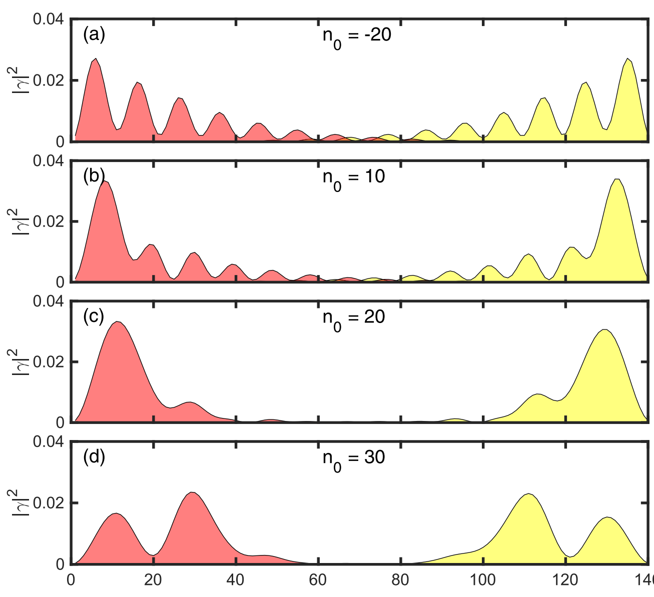

FIG. 40. Majorana components of the NSN system on the application of the ZMP to the topological state at $\Gamma > \Gamma_c$ with $\Gamma_0 = 1.4$ meV for different n_0 values. The Majorana components remain separated for a range of n_0 values.

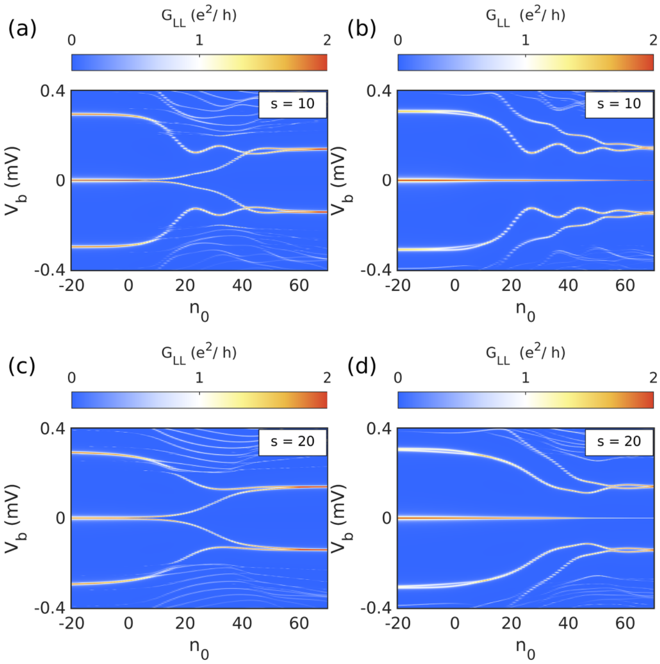

FIG. 41. Effect of smoothness on moving protocol: (a) trivial ZBP, $s = 10$; (b) topological ZBP, $s = 10$; (c) trivial ZBP, $s = 20$; and (d) topological ZBP, $s = 20$.

moving protocol. We present the results obtained from applying the moving protocol to an NSN heterostructure. Figure 41 illustrates both trivial and topological ZBPs in the NSN system under the influence of the moving protocol where we have utilized two different smoothness values.

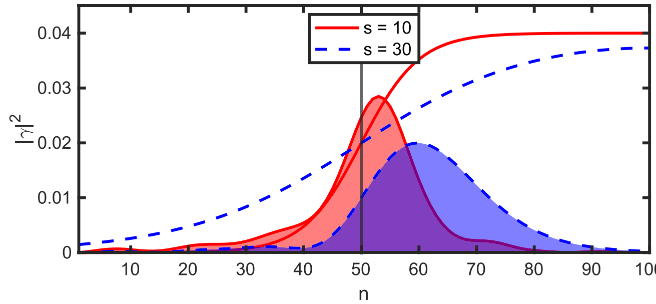

FIG. 42. Effect of smoothness on Majorana components shown here for a clean nanowire.

As anticipated, increasing the smoothness parameter leads to a smoother transition from the topological regime to the trivial regime. Upon comparing Figs. 41(a) and 41(b) with Figs. 41(c) and 41(d), it is evident that the primary observation of the moving protocol remains unaffected by the domain-wall width. Specifically, throughout the protocol, the topological ZBP remains at zero bias, while the trivial ZBP splits into two peaks at finite bias. However, taking too high a value of s will make the domain wall broad and destroy the trivial-topological- trivial structure.

Furthermore, it is worth noting that the domain-wall width also plays a role in determining the positions of the Majorana bound states within the system, particularly in response to the moving protocol. This relationship is evident from the observations presented in Fig. 42, where variations in the domain-wall width directly impact the positioning of the Majorana bound states.

[1] A. Y. Kitaev, Unpaired Majorana fermions in quantum wires, Phys. Usp. **44**, 131 (2001).
[2] C. Nayak, S. H. Simon, A. Stern, M. Freedman, and S. Das Sarma, Non-Abelian anyons and topological quantum computation, Rev. Mod. Phys. **80**, 1083 (2008).
[3] J. Alicea, New directions in the pursuit of Majorana fermions in solid state systems, Rep. Prog. Phys. **75**, 076501 (2012).
[4] S. D. Sarma, M. Freedman, and C. Nayak, Majorana zero modes and topological quantum computation, npj Quantum Inf. **1**, 15001 (2015).
[5] G. Moore and N. Read, Nonabelions in the fractional quantum Hall effect, Nucl. Phys. B **360**, 362 (1991).
[6] T. Rice and M. Sigrist, Sr_2RuO_4: An electronic analogue of ^{3}He?, J. Phys.: Condens. Matter **7**, L643 (1995).
[7] L. Fu and C. L. Kane, Superconducting proximity effect and Majorana fermions at the surface of a topological insulator, Phys. Rev. Lett. **100**, 096407 (2008).
[8] J. D. Sau, R. M. Lutchyn, S. Tewari, and S. D. Sarma, Generic new platform for topological quantum computation using semiconductor heterostructures, Phys. Rev. Lett. **104**, 040502 (2010).
[9] Y. Oreg, G. Refael, and F. von Oppen, Helical liquids and Majorana bound states in quantum wires, Phys. Rev. Lett. **105**, 177002 (2010).
[10] T. D. Stanescu, J. D. Sau, R. M. Lutchyn, and S. Das Sarma, Proximity effect at the superconductor-topological insulator interface, Phys. Rev. B **81**, 241310(R) (2010).
[11] S. M. Albrecht, A. P. Higginbotham, M. Madsen, F. Kuemmeth, T. S. Jespersen, J. Nygård, P. Krogstrup, and C. Marcus, Exponential protection of zero modes in Majorana islands, Nature (London) **531**, 206 (2016).
[12] H. O. H. Churchill, V. Fatemi, K. Grove-Rasmussen, M. T. Deng, P. Caroff, H. Q. Xu, and C. M. Marcus, Superconductor-nanowire devices from tunneling to the multichannel regime: Zero-bias oscillations and magnetoconductance crossover, Phys. Rev. B **87**, 241401(R) (2013).
[13] A. Das, Y. Ronen, Y. Most, Y. Oreg, M. Heiblum, and H. Shtrikman, Zero-bias peaks and splitting in an Al-InAs nanowire topological superconductor as a signature of Majorana fermions, Nat. Phys. **8**, 887 (2012).
[14] V. Mourik, K. Zuo, S. M. Frolov, S. Plissard, E. P. Bakkers, and L. P. Kouwenhoven, Signatures of Majorana fermions in hybrid superconductor-semiconductor nanowire devices, Science **336**, 1003 (2012).
[15] K. Sengupta, I. Žutić, H.-J. Kwon, V. M. Yakovenko, and S. Das Sarma, Midgap edge states and pairing symmetry of quasi-one-dimensional organic superconductors, Phys. Rev. B **63**, 144531 (2001).

[16] F. Setiawan, C.-X. Liu, J. D. Sau, and S. Das Sarma, Electron temperature and tunnel coupling dependence of zero-bias and almost-zero-bias conductance peaks in Majorana nanowires, Phys. Rev. B **96**, 184520 (2017).

[17] P. Yu, J. Chen, M. Gomanko, G. Badawy, E. P. Bakkers, K. Zuo, V. Mourik, and S. M. Frolov, Non-Majorana states yield nearly quantized conductance in proximatized nanowires, Nat. Phys. **17**, 482 (2021).

[18] H. Pan and S. D. Sarma, Physical mechanisms for zero-bias conductance peaks in Majorana nanowires, Phys. Rev. Res. **2**, 013377 (2020).

[19] A. Vuik, B. Nijholt, A. R. Akhmerov, and M. Wimmer, Reproducing topological properties with quasi-Majorana states, SciPost Phys. **7**, 061 (2019).

[20] H. Pan, W. S. Cole, J. D. Sau, and S. Das Sarma, Generic quantized zero-bias conductance peaks in superconductor-semiconductor hybrid structures, Phys. Rev. B **101**, 024506 (2020).

[21] J. Chen, B. D. Woods, P. Yu, M. Hocevar, D. Car, S. R. Plissard, E. P. A. M. Bakkers, T. D. Stanescu, and S. M. Frolov, Ubiquitous non-Majorana zero-bias conductance peaks in nanowire devices, Phys. Rev. Lett. **123**, 107703 (2019).

[22] B. D. Woods, J. Chen, S. M. Frolov, and T. D. Stanescu, Zero-energy pinning of topologically trivial bound states in multiband semiconductor-superconductor nanowires, Phys. Rev. B **100**, 125407 (2019).

[23] E. Vernek, P. H. Penteado, A. C. Seridonio, and J. C. Egues, Subtle leakage of a Majorana mode into a quantum dot, Phys. Rev. B **89**, 165314 (2014).

[24] A. Grivnin, E. Bor, M. Heiblum, Y. Oreg, and H. Shtrikman, Concomitant opening of a bulk-gap with an emerging possible Majorana zero mode, Nat. Commun. **10**, 1940 (2019).

[25] C. Moore, C. Zeng, T. D. Stanescu, and S. Tewari, Quantized zero-bias conductance plateau in semiconductor-superconductor heterostructures without topological Majorana zero modes, Phys. Rev. B **98**, 155314 (2018).

[26] Y. Huang, H. Pan, C. X. Liu, J. D. Sau, T. D. Stanescu, and S. D. Sarma, Metamorphosis of Andreev bound states into Majorana bound states in pristine nanowires, Phys. Rev. B **98**, 144511 (2018).

[27] F. Nichele, A. C. C. Drachmann, A. M. Whiticar, E. C. T. O'Farrell, H. J. Suominen, A. Fornieri, T. Wang, G. C. Gardner, C. Thomas, A. T. Hatke, P. Krogstrup, M. J. Manfra, K. Flensberg, and C. M. Marcus, Scaling of Majorana zero-bias conductance peaks, Phys. Rev. Lett. **119**, 136803 (2017).

[28] J. Kammhuber, M. C. Cassidy, F. Pei, M. P. Nowak, A. Vuik, O. Gül, D. Car, S. R. Plissard, E. P. Bakkers, M. Wimmer, and L. P. Kouwenhoven, Conductance through a helical state in an indium antimonide nanowire, Nat. Commun. **8**, 478 (2017).

[29] C. Reeg, O. Dmytruk, D. Chevallier, D. Loss, and J. Klinovaja, Zero-energy Andreev bound states from quantum dots in proximitized Rashba nanowires, Phys. Rev. B **98**, 245407 (2018).

[30] C. X. Liu, J. D. Sau, T. D. Stanescu, and S. Das Sarma, Andreev bound states versus Majorana bound states in quantum dot-nanowire-superconductor hybrid structures: Trivial versus topological zero-bias conductance peaks, Phys. Rev. B **96**, 075161 (2017).

[31] J. Cayao, E. Prada, P. San-Jose, and R. Aguado, SNS junctions in nanowires with spin-orbit coupling: Role of confinement and helicity on the subgap spectrum, Phys. Rev. B **91**, 024514 (2015).

[32] H. Zhang, Önder Gül, S. Conesa-Boj, M. P. Nowak, M. Wimmer, K. Zuo, V. Mourik, F. K. D. Vries, J. V. Veen, M. W. D. Moor, J. D. Bommer, D. J. V. Woerkom, D. Car, S. R. Plissard, E. P. Bakkers, M. Quintero-Pérez, M. C. Cassidy, S. Koelling, S. Goswami, K. Watanabe *et al.*, Ballistic superconductivity in semiconductor nanowires, Nat. Commun. **8**, 16025 (2017).

[33] A. P. Higginbotham, S. M. Albrecht, G. Kiršanskas, W. Chang, F. Kuemmeth, P. Krogstrup, T. S. Jespersen, J. Nygård, K. Flensberg, and C. M. Marcus, Parity lifetime of bound states in a proximitized semiconductor nanowire, Nat. Phys. **11**, 1017 (2015).

[34] O. Dmytruk, D. Loss, and J. Klinovaja, Pinning of Andreev bound states to zero energy in two-dimensional superconductor-semiconductor Rashba heterostructures, Phys. Rev. B **102**, 245431 (2020).

[35] C. X. Liu, J. D. Sau, and S. Das Sarma, Role of dissipation in realistic Majorana nanowires, Phys. Rev. B **95**, 054502 (2017).

[36] E. Prada, P. San-Jose, and R. Aguado, Transport spectroscopy of *ns* nanowire junctions with Majorana fermions, Phys. Rev. B **86**, 180503(R) (2012).

[37] E. J. H. Lee, X. Jiang, R. Aguado, G. Katsaros, C. M. Lieber, and S. De Franceschi, Zero-bias anomaly in a nanowire quantum dot coupled to superconductors, Phys. Rev. Lett. **109**, 186802 (2012).

[38] E. Prada, P. San-Jose, M. W. de Moor, A. Geresdi, E. J. Lee, J. Klinovaja, D. Loss, J. Nygård, R. Aguado, and L. P. Kouwenhoven, From Andreev to Majorana bound states in hybrid superconductor-semiconductor nanowires, Nat. Rev. Phys. **2**, 575 (2020).

[39] P. San-Jose, J. Cayao, E. Prada, and R. Aguado, Majorana bound states from exceptional points in non-topological superconductors, Sci. Rep. **6**, 21427 (2016).

[40] L. Rossi, F. Dolcini, and F. Rossi, Majorana-like localized spin density without bound states in topologically trivial spin-orbit coupled nanowires, Phys. Rev. B **101**, 195421 (2020).

[41] M. T. Deng, S. Vaitiekenas, E. B. Hansen, J. Danon, M. Leijnse, K. Flensberg, J. Nygård, P. Krogstrup, and C. M. Marcus, Majorana bound state in a coupled quantum-dot hybrid-nanowire system, Science **354**, 1557 (2016).

[42] H. Song, Z. Zhang, D. Pan, D. Liu, Z. Wang, Z. Cao, L. Liu, L. Wen, D. Liao, R. Zhuo, D. E. Liu, R. Shang, J. Zhao, and H. Zhang, Large zero bias peaks and dips in a four-terminal thin InAs-Al nanowire device, Phys. Rev. Res. **4**, 033235 (2022).

[43] J. Avila, F. Peñaranda, E. Prada, P. San-Jose, and R. Aguado, Non-Hermitian topology as a unifying framework for the Andreev versus Majorana states controversy, Commun. Phys. **2**, 133 (2019).

[44] J. Cayao and P. Burset, Confinement-induced zero-bias peaks in conventional superconductor hybrids, Phys. Rev. B **104**, 134507 (2021).

[45] M. Aghaee, A. Akkala, Z. Alam, R. Ali, A. A. Ramirez, M. Andrzejczuk, A. E. Antipov, M. Astafev, B. Bauer, J. Becker *et al.*, InAs-Al hybrid devices passing the topological gap protocol, Phys. Rev. B **107**, 245423 (2023).

[46] C. Moore, T. D. Stanescu, and S. Tewari, Two-terminal charge tunneling: Disentangling Majorana zero modes from partially separated Andreev bound states in semiconductor-superconductor heterostructures, Phys. Rev. B **97**, 165302 (2018).

[47] T. D. Stanescu and S. Tewari, Robust low-energy Andreev bound states in semiconductor-superconductor structures: Importance of partial separation of component Majorana bound states, Phys. Rev. B **100**, 155429 (2019).

[48] P. Marra and A. Nigro, Majorana/Andreev crossover and the fate of the topological phase transition in inhomogeneous nanowires, J. Phys.: Condens. Matter **34**, 124001 (2022).

[49] H. Pan, J. D. Sau, and S. Das Sarma, Three-terminal nonlocal conductance in Majorana nanowires: Distinguishing topological and trivial in realistic systems with disorder and inhomogeneous potential, Phys. Rev. B **103**, 014513 (2021).

[50] R. Hess, H. F. Legg, D. Loss, and J. Klinovaja, Local and nonlocal quantum transport due to Andreev bound states in finite Rashba nanowires with superconducting and normal sections, Phys. Rev. B **104**, 075405 (2021).

[51] R. V. Mishmash, B. Bauer, F. von Oppen, and J. Alicea, Dephasing and leakage dynamics of noisy Majorana-based qubits: Topological versus andreev, Phys. Rev. B **101**, 075404 (2020).

[52] Y.-H. Lai, S. D. Sarma, and J. D. Sau, Quality factor for zero-bias conductance peaks in Majorana nanowire, Phys. Rev. B **106**, 094504 (2022).

[53] O. A. Awoga, J. Cayao, and A. M. Black-Schaffer, Supercurrent detection of topologically trivial zero-energy states in nanowire junctions, Phys. Rev. Lett. **123**, 117001 (2019).

[54] J. Cayao and A. M. Black-Schaffer, Distinguishing trivial and topological zero-energy states in long nanowire junctions, Phys. Rev. B **104**, L020501 (2021).

[55] L. Baldo, L. G. Da Silva, A. M. Black-Schaffer, and J. Cayao, Zero-frequency supercurrent susceptibility signatures of trivial and topological zero-energy states in nanowire junctions, Supercond. Sci. Technol. **36**, 034003 (2023).

[56] J. Alicea, Y. Oreg, G. Refael, F. Von Oppen, and M. Fisher, Non-Abelian statistics and topological quantum information processing in 1D wire networks, Nat. Phys. **7**, 412 (2011).

[57] B. Bauer, T. Karzig, R. V. Mishmash, A. E. Antipov, and J. Alicea, Dynamics of Majorana-based qubits operated with an array of tunable gates, SciPost Phys. **5**, 004 (2018).

[58] Y. Hu, Z. Cai, M. A. Baranov, and P. Zoller, Majorana fermions in noisy Kitaev wires, Phys. Rev. B **92**, 165118 (2015).

[59] P. Zhang and F. Nori, Majorana bound states in a disordered quantum dot chain, New J. Phys. **18**, 043033 (2016).

[60] Typically, when constructing Majorana components, one could introduce opposite phase factors to the particle-hole pair. However, the selection of these phase factors should aim to minimize the spatial overlap between the resulting Majorana components, ensuring they are better suited for in-depth Majorana component analysis.

[61] S. K. Kim, S. Tewari, and Y. Tserkovnyak, Control and braiding of Majorana fermions bound to magnetic domain walls, Phys. Rev. B **92**, 020412(R) (2015).

[62] D. Aasen, M. Hell, R. V. Mishmash, A. Higginbotham, J. Danon, M. Leijnse, T. S. Jespersen, J. A. Folk, C. M. Marcus, K. Flensberg, and J. Alicea, Milestones toward Majorana-based quantum computing, Phys. Rev. X **6**, 031016 (2016).

[63] J. Li, T. Neupert, B. A. Bernevig, and A. Yazdani, Manipulating Majorana zero modes on atomic rings with an external magnetic field, Nat. Commun. **7**, 10395 (2016).

[64] G. L. Fatin, A. Matos-Abiague, B. Scharf, and I. Žutić, Wireless Majorana bound states: From magnetic tunability to braiding, Phys. Rev. Lett. **117**, 077002 (2016).

[65] P. Marra and M. Cuoco, Controlling Majorana states in topologically inhomogeneous superconductors, Phys. Rev. B **95**, 140504(R) (2017).

[66] K. R. Sapkota, S. Eley, E. Bussmann, C. T. Harris, L. N. Maurer, and T. M. Lu, Creation of nanoscale magnetic fields using nanomagnet arrays, AIP Adv. **9**, 075203 (2019).

[67] T. Zhou, N. Mohanta, J. E. Han, A. Matos-Abiague, and I. Žutić, Tunable magnetic textures in spin valves: From spintronics to Majorana bound states, Phys. Rev. B **99**, 134505 (2019).

[68] Y. Liu, S. Vaitiekenas, S. Martí-Sánchez, C. Koch, S. Hart, Z. Cui, T. Kanne, S. A. Khan, R. Tanta, S. Upadhyay *et al.*, Semiconductor–ferromagnetic insulator–superconductor nanowires: Stray field and exchange field, Nano Lett. **20**, 456 (2020).

[69] Z. Yang, B. Heischmidt, S. Gazibegovic, G. Badawy, D. Car, P. A. Crowell, E. P. Bakkers, and V. S. Pribiag, Spin transport in ferromagnet-InSb nanowire quantum devices, Nano Lett. **20**, 3232 (2020).

[70] P. Markos and C. M. Soukoulis, *Wave Propagation: From Electrons to Photonic Crystals and Left-Handed Materials* (Princeton University Press, Princeton, NJ, 2008).

[71] T.-P. Choy, J. M. Edge, A. R. Akhmerov, and C. W. J. Beenakker, Majorana fermions emerging from magnetic nanoparticles on a superconductor without spin-orbit coupling, Phys. Rev. B **84**, 195442 (2011).

[72] A. R. Akhmerov, J. P. Dahlhaus, F. Hassler, M. Wimmer, and C. W. J. Beenakker, Quantized conductance at the Majorana phase transition in a disordered superconducting wire, Phys. Rev. Lett. **106**, 057001 (2011).

[73] I. C. Fulga, F. Hassler, A. R. Akhmerov, and C. W. J. Beenakker, Scattering formula for the topological quantum number of a disordered multimode wire, Phys. Rev. B **83**, 155429 (2011).

[74] B. M. Fregoso, A. M. Lobos, and S. Das Sarma, Electrical detection of topological quantum phase transitions in disordered Majorana nanowires, Phys. Rev. B **88**, 180507(R) (2013).

[75] A. M. Lobos and S. D. Sarma, Tunneling transport in NSN Majorana junctions across the topological quantum phase transition, New J. Phys. **17**, 065010 (2015).